

See discussions, stats, and author profiles for this publication at: <https://www.researchgate.net/publication/6477125>

Spin Crossover in a Series of Iron(II) Complexes of 2-(2-Alkyl-2 H -tetrazol-5-yl)-1,10-phenanthroline: Effects of Alkyl Side Chain, Solvent, and Anion

ARTICLE *in* INORGANIC CHEMISTRY · MAY 2007

Impact Factor: 4.76 · DOI: 10.1021/ic062062h · Source: PubMed

CITATIONS

52

READS

61

6 AUTHORS, INCLUDING:



Fei Zhao

Qingdao University of Science and Technology

41 PUBLICATIONS 851 CITATIONS

SEE PROFILE



Tao Liu

Dalian University of Technology

59 PUBLICATIONS 1,241 CITATIONS

SEE PROFILE



Song Gao

Peking University

490 PUBLICATIONS 16,360 CITATIONS

SEE PROFILE

Spin Crossover in a Series of Iron(II) Complexes of 2-(2-Alkyl-2H-tetrazol-5-yl)-1,10-phenanthroline: Effects of Alkyl Side Chain, Solvent, and Anion

Wen Zhang, Fei Zhao, Tao Liu, Mei Yuan, Zhe-Ming Wang,* and Song Gao*

Beijing National Laboratory for Molecular Sciences, State Key Laboratory of Rare Earth Materials Chemistry and Applications, College of Chemistry and Molecular Engineering, Peking University, Beijing 100871, China

Received October 27, 2006

2-(2H-Tetrazol-5-yl)-1,10-phenanthroline (HL^0), its alkyl-substituted derivatives (L^n , where $n = 1-8, 10, 12, 14$, and 16 , denoting the carbon atom number of the alkyl chain) at the 2H position of the tetrazole ring, and their iron(II) complexes (**a** for $[Fe(L^0)_2]$, **na** for $[Fe(L^n)_2](ClO_4)_2$, and **nb** for $[Fe(L^n)_2](BF_4)_2$) were synthesized and characterized. The crystal structures of **a**, **a**·CH₃OH, **1a**·CH₃OH, **1b**·CH₃OH·CH₃CN, **2a**·H₂O, **2b**·H₂O, **4b**·CH₃OH, **5a**·H₂O, **5b**·H₂O, **6a**, **6b**, **7a**, **7b**, and **16a** are described, along with thermal analyses. **a** undergoes an abrupt spin crossover (SCO) at 255 K with a hysteresis loop of 6 K. **a**·CH₃OH, **2a**·H₂O, and **2b**·H₂O exhibit irreversible SCO behaviors due to the loss of solvent molecules upon heating. **3a**, **3b**, **4a**, and **5a**·H₂O show simple spin transitions above 350 K. The desolvated samples of **4b**·CH₃OH and **5b**·H₂O undergo two-step spin transitions. **16a** exhibits a two-step SCO behavior between 100 and 300 K, corresponding to sequential phase transitions from the low-spin (LS) phase to the intermediate phase and then to the high-spin phase, respectively, proved by crystal structure analysis and ⁵⁷Fe Mössbauer spectroscopy. **1a**·CH₃OH, **10a**, **10b**, **12a**, **12b**, **14a**, **14b**, and **16b** show gradual and incomplete SCO behaviors after cooling down from 400 K. **1b**·CH₃OH·CH₃CN, **6a**, **6b**, **7a**, **7b**, **8a**, and **8b** remain in the LS state even at 400 K. This proves that the alkyl side chains, together with the solvent molecules and anions, play a crucial role in the complicated SCO behaviors in this system.

Introduction

Some six-coordinate iron(II) coordination compounds, mostly those with an Fe–N₆ coordination environment, show a reversible spin crossover (SCO) between the diamagnetic low-spin (LS; $S = 0$) state and the paramagnetic high-spin (HS; $S = 2$) state by an external perturbation, such as temperature, pressure, or light irradiation.¹ As one of the best examples of molecular bistability, SCO complexes have been widely investigated over the last several decades because of

their potential applications in information storage, molecular switches, molecular electronics, and optical devices.² It is generally accepted that SCO arises not only from the well-designed ligand with a proper ligand-field strength but also from crystal packing, through which various kinds of intra- and intermolecular cooperative interactions, including covalent linkage among metal active sites,³ hydrogen-bonding,⁴ π – π stacking,⁵ and van der Waals interactions,⁶ exert great influences on SCO behaviors. In order to be used as an active element in molecular devices, SCO must be abrupt with a relatively large thermal hysteresis and centered around ambient temperature.^{2d} However, there is a long way to go in order to acquire the desired SCO properties because the

* To whom correspondence should be addressed. E-mail: zmw@pku.edu.cn (Z.-M.W.), gaosong@pku.edu.cn (S.G.). Tel: +86-10-62756320. Fax: +86-10-62751708.

(1) For reviews, see: (a) Goodwin, H. A. *Coord. Chem. Rev.* **1976**, *18*, 293. (b) König, E.; Ritter, G.; Kulshreshtha, S. K. *Chem. Rev.* **1985**, *85*, 219. (c) Toftlund, H. *Coord. Chem. Rev.* **1989**, *94*, 67. (d) Gülich, P. *Struct. Bonding (Berlin)* **1981**, *44*, 83. (e) Gülich, P.; Hauser, A. *Coord. Chem. Rev.* **1990**, *97*, 1. (f) König, E. *Struct. Bonding (Berlin)* **1991**, *76*, 51. (g) Kahn, O. *Molecular Magnetism*; VCH Publishers: New York, 1993; pp 1–86. (h) Gülich, P.; Hauser, A.; Spiering, H. *Angew. Chem., Int. Ed. Engl.* **1994**, *33*, 2024. (i) Gülich, P.; Garcia, Y.; Goodwin, H. A. *Chem. Soc. Rev.* **2000**, *29*, 419. (j) Gülich, P.; Goodwin, H. A. (Editors) *Top. Curr. Chem.* **2004**, *233*–235.

(2) (a) Kahn, O.; Launay, J. P. *Chemtronics* **1988**, *3*, 140. (b) Kahn, O.; Kröber, J.; Jay, C. *Adv. Mater.* **1992**, *4*, 718. (c) Gatteschi, D. *Adv. Mater.* **1994**, *6*, 635. (d) Kahn, O.; Martinez, C. *J. Science* **1998**, *279*, 44. (e) Muller, R. N.; Vander Elst, L.; Laurent, S. *J. Am. Chem. Soc.* **2003**, *125*, 8405.

(3) Real, J. A.; Gaspar, A. B.; Niel, V.; Muñoz, M. C. *Coord. Chem. Rev.* **2003**, *236*, 121 and references cited therein.

occurrence and types of SCO are neither predictable nor controllable in most cases.

Among the factors to affect SCO behavior, i.e., the ligand,¹ the counterion,⁷ and the solvent molecule,⁸ ligand modification is presently the most practicable approach to tuning SCO properties. It may not only directly tune the ligand-field strength but also largely change the crystal packing. Several investigations have been directed to the field of tuning SCO by ligand modification recently.^{9–20} Although some specific conclusions have been drawn from these studies, there is a lack of systematic synthesis and detailed measurements of properties and crystal structures, through which the com-

monly overlapped effects of ligand, solvent, and counterion on SCO could be elucidated separately and the often-encountered exceptions can be excluded from the regular species.

Up to now there have been over 200 SCO systems reported,²¹ in which the ligands are practically composed of not more than 20 structural units,^{1j} such as pyrazole, imidazole, thiazole, triazole, tetrazole, pyridine, pyrimidine, pyrazine, phenanthroline, imine, amine, phenolate, etc. These basic units possess moderate ligand-field strengths to induce SCO of an iron(II) or iron(III) ion in a measurable temperature range. In exploration for new SCO systems, it is a convenient and practicable way to combine the units together to afford new SCO systems, which is demonstrated by various SCO systems.^{1j} More importantly, once the SCO ligand contains some sites for easy modification, it will open a new way to finely tune the electronic and geometric structures of the ligand and eventually the SCO properties. Following this strategy, 2-(2*H*-tetrazol-5-yl)-1,10-phenanthroline is designed, which includes two basic SCO components, i.e., tetrazole and 1,10-phenanthroline. Similar tridentate ligands, such as oxadiazole,²² thiazole,²³ imidazole,²⁴ pyrazole,²⁵ or triazole²⁶ attached with 1,10-phenanthroline, have been reported by Goodwin et al., but only simple SCO properties are observed in the corresponding isolated iron(II) complexes. Herein, we report the syntheses and characterizations of an extensive series of iron(II) complexes using 2-(2*H*-tetrazol-5-yl)-1,10-phenanthroline and its alkyl-substituted derivatives as ligands. We will show how variation of the alkyl side chains as well as the crystallized solvent molecules and anions changes the crystal packing and further affects the SCO behaviors significantly.

Experimental Section

General Procedures. All reagents and solvents in the syntheses were of reagent grade and used without further purification. (**Caution!** Sodium azide and iron(II) perchlorate are potentially explosive and should be handled with much care.) Elemental analyses of carbon, hydrogen, and nitrogen were carried out with an Elemental Vario EL analyzer. Micro-IR spectroscopy studies were performed on a Nicolet Magna-IR 750 spectrophotometer in the 4000–650 cm⁻¹ region (w, weak; b, broad; m, medium; s, strong). ¹H and ¹³C NMR spectra were recorded on a Varian YH200 spectrometer (s, singlet; d, doublet; t, triplet; m, multiplet; dd, double doublet). Thermal analyses were performed on a DuPont 1090B, or a SDT Q600 thermal analyzer (thermogravimetric analysis/differential thermal analysis, TGA/DTA) and a Q100 differential scanning calorimeter (DSC), under a dinitrogen gas flow (50 mL min⁻¹) with a constant heating or cooling rate of 5 K min⁻¹. Powder

- (4) (a) Sunatsuki, Y.; Ikuta, Y.; Matsumoto, N.; Ohta, H.; Kojima, M.; Iijima, S.; Hayami, S.; Maeda, Y.; Kaizaki, S.; Dahan, F.; Tuchagues, J.-P. *Angew. Chem., Int. Ed.* **2003**, *42*, 1614. (b) Ikuta, Y.; Ooidemizu, M.; Yamahata, Y.; Yamada, M.; Osa, S.; Matsumoto, N.; Iijima, S.; Sunatsuki, Y.; Kojima, M.; Dahan, F.; Tuchagues, J.-P. *Inorg. Chem.* **2003**, *42*, 7001. (c) Yamada, M.; Ooidemizu, M.; Ikuta, Y.; Osa, S.; Matsumoto, N.; Iijima, S.; Kojima, M.; Dahan, F.; Tuchagues, J.-P. *Inorg. Chem.* **2003**, *42*, 8406. (d) Matouzenko, G. S.; Molnar, G.; Brefuel, N.; Perrin, M.; Bousseksou, A.; Borshch, S. A. *Chem. Mater.* **2003**, *15*, 550.
- (5) (a) Real, J. A.; Gallois, B.; Granier, T.; Suez-Panamá, F.; Zarembowitch, J. *Inorg. Chem.* **1992**, *31*, 4972. (b) Létard, J. F.; Guionneau, P.; Codjovi, E.; Lavastre, O.; Bravic, G.; Chasseau, D.; Kahn, O. *J. Am. Chem. Soc.* **1997**, *119*, 10861. (c) Zhong, Z.-J.; Tao, J.-Q.; Yu, Z.; Duan, C.-Y.; Liu, Y.-J.; You, X.-Z. *J. Chem. Soc., Dalton Trans.* **1998**, 327. (d) Hayami, S.; Gu, Z.-Z.; Shiro, M.; Einaga, Y.; Fujishima, A.; Sato, O. *J. Am. Chem. Soc.* **2000**, *122*, 7126. (e) Boča, R.; Boča, M.; Dlháň, L.; Falk, K.; Fuess, H.; Haase, W.; Jaroščíak, R.; Papánková, B.; Renz, F.; Vrbová, M.; Werner, R. *Inorg. Chem.* **2001**, *40*, 3025.
- (6) (a) Arata, S.; Torigoe, H.; Iihoshi, T.; Matsumoto, N.; Dahan, F.; Tuchagues, J.-P. *Inorg. Chem.* **2005**, *44*, 9288. (b) Hayami, S.; Shigeyoshi, Y.; Akita, M.; Inoue, K.; Kato, K.; Osaka, K.; Takata, M.; Kawajiri, R.; Mitani, T.; Maeda, Y. *Angew. Chem., Int. Ed.* **2005**, *44*, 4899.
- (7) (a) Gaspar, A. B.; Muñoz, M. C.; Niel, V.; Real, J. A. *Inorg. Chem.* **2001**, *40*, 9. (b) Brewer, C.; Brewer, G.; Luckett, C.; Marbury, G. S.; Viragh, C.; Beatty, A. M.; Scheidt, W. R. *Inorg. Chem.* **2004**, *43*, 2402. (c) Tuna, F.; Lees, M. R.; Clarkson, G. J.; Hannon, M. J. *Chem.—Eur. J.* **2004**, *10*, 5737. (d) Galet, A.; Gaspar, A. B.; Muñoz, M. C.; Real, J. A. *Inorg. Chem.* **2006**, *45*, 4413. (e) Lemerrier, G.; Bréfuel, N.; Shova, S.; Wolny, J. A.; Dahan, F.; Verelst, M.; Paulsen, H.; Trautwein, A. X.; Tuchagues, J.-P. *Chem.—Eur. J.* **2006**, *12*, 7421.
- (8) (a) Halder, G. J.; Kepert, C. J.; Moubarak, B.; Murray, K. S.; Cashion, J. D. *Science* **2002**, *298*, 1762. (b) Niel, V.; Thompson, A. L.; Muñoz, M. C.; Galet, A.; Goeta, A. E.; Real, J. A. *Angew. Chem., Int. Ed.* **2003**, *42*, 3760. (c) Hayami, S.; Hashiguchi, K.; Juhász, G.; Ohba, M.; Okawa, H.; Maeda, Y.; Kato, K.; Osaka, K.; Takata, M.; Inoue, K. *Inorg. Chem.* **2004**, *43*, 4124. (d) Hostettler, M.; Törnroos, K. W.; Chernyshov, D.; Vangdal, B.; Bürgi, H.-B. *Angew. Chem., Int. Ed.* **2004**, *43*, 4589.
- (9) Constable, E. C.; Baum, G.; Bill, E.; Dyson, R.; van Eldik, R.; Fenske, D.; Kaderli, S.; Morris, D.; Neubrand, A.; Neuburger, M.; Smith, D. R.; Wieghardt, K.; Zehnder, M.; Zuberbühler, A. D. *Chem.—Eur. J.* **1999**, *5*, 498.
- (10) Ksenofontov, V.; Levchenko, G.; Spiering, H.; Gütlich, P.; Letard, J.-F.; Bouhedja, Y.; Kahn, O. *Chem. Phys. Lett.* **1998**, *294*, 545.
- (11) Roubeau, O.; Gomez, J. M. A.; Balskus, E.; Kolnaar, J. J. A.; Haasnoot, J. G.; Reedijk, J. *New J. Chem.* **2001**, *25*, 144.
- (12) Stassen, A. F.; Grunert, M.; Dova, E.; Müller, M.; Weinberger, P.; Wiesinger, G.; Schenk, H.; Linert, W.; Haasnoot, J. G.; Reedijk, J. *Eur. J. Inorg. Chem.* **2003**, 2273.
- (13) Li, M.; Bonnet, D.; Bill, E.; Neese, F.; Weyhermüller, T.; Blum, N.; Sellmann, D.; Wieghardt, K. *Inorg. Chem.* **2002**, *41*, 3444.
- (14) Goodwin, H. A. *Top. Curr. Chem.* **2004**, *233*, 59.
- (15) Mukherjee, S.; Weyhermüller, T.; Bill, E.; Wieghardt, K.; Chaudhuri, P. *Inorg. Chem.* **2005**, *44*, 7099.
- (16) Salmon, L.; Bousseksou, A.; Donnadieu, B.; Tuchagues, J.-P. *Inorg. Chem.* **2005**, *44*, 1763.
- (17) Reger, D. L.; Gardinier, J. R.; Gemmill, W. R.; Smith, M. D.; Shahin, A. M.; Long, G. J.; Rebbouh, L.; Grandjean, F. *J. Am. Chem. Soc.* **2005**, *127*, 2303.
- (18) Hitomi, Y.; Higuchi, M.; Minami, H.; Tanaka, T.; Funabiki, T. *Chem. Commun.* **2005**, 1758.
- (19) Nakano, K.; Suemura, N.; Yoneda, K.; Kawata, S.; Kaizaki, S. *Dalton Trans.* **2005**, 740.
- (20) Boča, R.; Renz, F.; Boča, M.; Fuess, H.; Haase, W.; Kickelbick, G.; Linert, W.; Vrbová-Schikora, M. *Inorg. Chem. Commun.* **2005**, *8*, 227.
- (21) Bousseksou, A.; Molnár, G.; Matouzenko, G. *Eur. J. Inorg. Chem.* **2004**, 4353.
- (22) Goodwin, H. A.; Smith, F. E. *Inorg. Nucl. Chem. Lett.* **1974**, *10*, 99.
- (23) Goodwin, H. A.; Mather, D. W.; Smith, F. E. *Aust. J. Chem.* **1975**, *28*, 33.
- (24) Mather, D. W.; Goodwin, H. A. *Aust. J. Chem.* **1975**, *28*, 505.
- (25) Abushamleh, A. S.; Goodwin, H. A. *Aust. J. Chem.* **1988**, *41*, 873.
- (26) Sugiyarto, K. H.; Craig, D. C.; Rae, A. D.; Goodwin, H. A. *Aust. J. Chem.* **1996**, *49*, 505.

X-ray diffraction (PXRD) patterns of the samples were collected with a Rigaku D/Max2000 diffractometer equipped with Cu K α radiation ($\lambda = 1.5418 \text{ \AA}$).

2-(2H-Tetrazol-5-yl)-1,10-phenanthroline, HL⁰. The ligand was prepared according to a literature method.²⁷ 2-Cyano-1,10-phenanthroline²⁸ (410 mg, 2.0 mmol), NH₄Cl (135 mg, 2.5 mmol), and NaN₃ (160 mg, 2.5 mmol) in *N,N*-dimethylformamide (10 mL) were stirred and heated at 140 °C for 48 h. The cooled mixture was poured into H₂O (200 mL) and filtered. The filtrate was acidified to pH = 2 with concentrated hydrochloric acid. After stirring for 5 h, the suspension was filtered. The resulting solid was washed with H₂O (2 \times 5 mL) and dried in vacuum over P₂O₅ at room temperature. Yield: 54%. FT-IR (cm⁻¹): 3392 (m), 3069 (m), 1602 (s), 1545 (s), 1418 (w), 867 (m), 727 (w). ¹H NMR (200 MHz, CDCl₃): δ 9.06 (dd, $J = 4.8 \text{ Hz}$, 1H), 8.64 (d, $J = 8.6 \text{ Hz}$, 1H), 8.48 (d, $J = 8.2 \text{ Hz}$, 1H), 8.39 (dd, $J = 8.2 \text{ Hz}$, 1H), 7.92 (s, 2H), 7.75 (dd, $J = 8.2 \text{ Hz}$, 1H). Anal. Calcd for C₁₃H₈N₆·1.5H₂O: C, 56.72; H, 4.03; N, 30.53. Found: C, 56.92; H, 3.64; N, 30.76.

Compounds Lⁿ were prepared by a similar method as follows. To a suspension of HL⁰ (1.25 g, 5.0 mmol) was added powdered KOH (400 mg, 7.0 mmol) in *n*-propanol (150 mL). After heating at 60–80 °C for 1 h, a solution of 7 mmol of alkyl bromide (as to L¹, methyl iodide was used) in *n*-propanol (20 mL) was added. After reaction for 48 h and removal of the solvent, the mixture was treated with an aqueous KOH solution (400 mg, 7.0 mmol) and then extracted twice with chloroform (2 \times 20 mL). The solvent was then evaporated, and the residual was eluted with petroleum ether (60–90 °C) and then ethyl acetate on a column filled with silica gel. The second eluting part was collected and concentrated to afford the desired compound.

2-(2-Methyl-2H-tetrazol-5-yl)-1,10-phenanthroline, L¹. Yield: 34%. FT-IR (cm⁻¹): 3050 (w), 1555 (m), 1497 (s), 1419 (s), 1154 (m), 857 (s), 738 (s). ¹H NMR (200 MHz, CDCl₃): δ 9.27 (dd, $J = 4.2 \text{ Hz}$, 1H), 8.56 (d, $J = 8.6 \text{ Hz}$, 1H), 8.41 (d, $J = 8.4 \text{ Hz}$, 1H), 8.25 (dd, $J = 8.2 \text{ Hz}$, 1H), 7.83 (s, 2H), 7.65 (dd, $J = 8.0 \text{ Hz}$, 1H), 4.52 (s, 3H). ¹³C NMR (50 MHz, CDCl₃): δ 165.04, 150.69, 146.55, 146.16, 145.95, 137.11, 135.81, 128.89, 128.82, 127.55, 125.95, 123.18, 121.44, 39.66. Anal. Calcd for C₁₄H₁₀N₆: C, 64.11; H, 3.84; N, 32.04. Found: C, 63.81; H, 4.12; N, 32.43.

2-(2-Ethyl-2H-tetrazol-5-yl)-1,10-phenanthroline, L². Yield: 68%. FT-IR (cm⁻¹): 3064 (w), 2987 (w), 2939 (w), 1494 (m), 1414 (s), 1152 (m), 851 (s), 736 (m). ¹H NMR (200 MHz, CDCl₃): δ 9.26 (dd, $J = 4.4 \text{ Hz}$, 1H), 8.60 (d, $J = 8.2 \text{ Hz}$, 1H), 8.44 (d, $J = 8.6 \text{ Hz}$, 1H), 8.28 (dd, $J = 8.2 \text{ Hz}$, 1H), 7.86 (s, 2H), 7.67 (dd, $J = 8.2 \text{ Hz}$, 1H), 4.84 (quad, $J = 7.6 \text{ Hz}$, 2H), 1.77 (t, $J = 7.4 \text{ Hz}$, 3H). ¹³C NMR (50 MHz, CDCl₃): δ 164.99, 150.83, 146.96, 146.33, 146.11, 137.21, 135.91, 128.98, 128.92, 127.61, 126.09, 123.25, 121.68, 48.66, 14.52. Anal. Calcd for C₁₅H₁₂N₆: C, 65.21; H, 4.38; N, 30.42. Found: C, 64.79; H, 4.37; N, 30.68.

2-(2-*n*-Propyl-2H-tetrazol-5-yl)-1,10-phenanthroline, L³. Yield: 58%. FT-IR (cm⁻¹): 3058 (w), 2964 (m), 2937 (w), 2878 (w), 1496 (m), 1399 (s), 1050 (m), 854 (s), 735 (m). ¹H NMR (200 MHz, CDCl₃): δ 9.26 (dd, $J = 4.4 \text{ Hz}$, 1H), 8.57 (d, $J = 8.6 \text{ Hz}$, 1H), 8.39 (d, $J = 8.2 \text{ Hz}$, 1H), 8.24 (dd, $J = 7.8 \text{ Hz}$, 1H), 7.81 (s, 2H), 7.64 (dd, $J = 8.2 \text{ Hz}$, 1H), 4.74 (t, $J = 7.2 \text{ Hz}$, 2H), 2.20 (m, $J = 7.2 \text{ Hz}$, 2H), 1.03 (t, $J = 7.2 \text{ Hz}$, 3H). ¹³C NMR (50 MHz, CDCl₃): δ 164.80, 150.61, 146.79, 146.15, 145.95, 137.03, 135.75, 128.81, 128.77, 127.44, 125.93, 123.10, 121.55, 54.94, 22.64, 10.88.

Anal. Calcd for C₁₆H₁₄N₆: C, 66.19; H, 4.86; N, 28.95. Found: C, 65.84; H, 4.80; N, 29.23.

2-(2-*n*-Butyl-2H-tetrazol-5-yl)-1,10-phenanthroline, L⁴. Yield: 32%. FT-IR (cm⁻¹): 3069 (w), 2961 (s), 2942 (w), 2872 (w), 1494 (m), 1418 (s), 1048 (m), 866 (s), 738 (m). ¹H NMR (200 MHz, CDCl₃): δ 9.27 (dd, $J = 4.4 \text{ Hz}$, 1H), 8.58 (d, $J = 8.2 \text{ Hz}$, 1H), 8.41 (d, $J = 8.2 \text{ Hz}$, 1H), 8.25 (dd, $J = 8.2 \text{ Hz}$, 1H), 7.83 (s, 2H), 7.65 (dd, $J = 8.2 \text{ Hz}$, 1H), 4.78 (t, $J = 7.2 \text{ Hz}$, 2H), 2.15 (m, $J = 7.2 \text{ Hz}$, 2H), 1.44 (m, $J = 7.6 \text{ Hz}$, 2H), 0.99 (t, $J = 7.2 \text{ Hz}$, 3H). ¹³C NMR (50 MHz, CDCl₃): δ 164.90, 150.76, 146.92, 146.27, 146.06, 137.13, 135.82, 128.89, 128.84, 127.53, 126.00, 123.16, 121.62, 53.11, 31.02, 19.45, 13.17. Anal. Calcd for C₁₇H₁₆N₆: C, 67.09; H, 5.30; N, 27.61. Found: C, 67.02; H, 5.30; N, 27.40.

2-(2-*n*-Pentyl-2H-tetrazol-5-yl)-1,10-phenanthroline, L⁵. Yield: 36%. FT-IR (cm⁻¹): 3046 (w), 2956 (s), 2931 (w), 2873 (w), 1496 (m), 1403 (s), 1047 (m), 861 (s), 740 (m). ¹H NMR (200 MHz, CDCl₃): δ 9.23 (dd, $J = 4.4 \text{ Hz}$, 1H), 8.55 (d, $J = 8.2 \text{ Hz}$, 1H), 8.40 (d, $J = 8.2 \text{ Hz}$, 1H), 8.27 (dd, $J = 8.2 \text{ Hz}$, 1H), 7.82 (s, 2H), 7.66 (dd, $J = 8.2 \text{ Hz}$, 1H), 4.78 (t, $J = 7.2 \text{ Hz}$, 2H), 2.17 (m, $J = 7.2 \text{ Hz}$, 2H), 1.39 (m, 4H), 0.94 (t, $J = 6.8 \text{ Hz}$, 3H). ¹³C NMR (50 MHz, CDCl₃): δ 164.82, 150.26, 146.45, 145.91, 145.73, 137.11, 136.17, 128.94, 128.90, 127.47, 126.09, 123.31, 121.55, 53.54, 28.89, 28.36, 21.88, 13.70. Anal. Calcd for C₁₈H₁₈N₆: C, 67.90; H, 5.70; N, 26.40. Found: C, 67.19; H, 5.79; N, 26.71.

2-(2-*n*-Hexyl-2H-tetrazol-5-yl)-1,10-phenanthroline, L⁶. Yield: 56%. FT-IR (cm⁻¹): 3055 (w), 2953 (s), 2922 (w), 2859 (w), 1492 (m), 1403 (s), 1047 (m), 874 (s), 740 (m). ¹H NMR (200 MHz, CDCl₃): δ 9.26 (dd, $J = 4.4 \text{ Hz}$, 1H), 8.58 (d, $J = 8.2 \text{ Hz}$, 1H), 8.40 (d, $J = 8.2 \text{ Hz}$, 1H), 8.25 (dd, $J = 8.0 \text{ Hz}$, 1H), 7.82 (s, 2H), 7.64 (dd, $J = 7.8 \text{ Hz}$, 1H), 4.77 (t, $J = 7.2 \text{ Hz}$, 2H), 2.16 (m, $J = 7.2 \text{ Hz}$, 2H), 1.36 (m, 6H), 0.99 (t, $J = 7.2 \text{ Hz}$, 3H). ¹³C NMR (50 MHz, CDCl₃): δ 164.81, 150.70, 146.86, 146.21, 146.01, 137.08, 135.78, 128.86, 128.81, 127.50, 125.97, 123.14, 121.60, 53.45, 31.37, 29.16, 28.42, 26.22, 22.35, 13.87. Anal. Calcd for C₁₉H₂₀N₆: C, 68.65; H, 6.06; N, 25.28. Found: C, 68.30; H, 6.11; N, 25.09.

2-(2-*n*-Heptyl-2H-tetrazol-5-yl)-1,10-phenanthroline, L⁷. Yield: 62%. FT-IR (cm⁻¹): 3054 (w), 2954 (s), 2928 (m), 2866 (w), 1494 (m), 1405 (s), 1048 (m), 861 (s), 739 (m). ¹H NMR (200 MHz, CDCl₃): δ 9.26 (dd, $J = 4.4 \text{ Hz}$, 1H), 8.57 (d, $J = 8.2 \text{ Hz}$, 1H), 8.40 (d, $J = 8.2 \text{ Hz}$, 1H), 8.25 (dd, $J = 8.2 \text{ Hz}$, 1H), 7.82 (s, 2H), 7.64 (dd, $J = 8.0 \text{ Hz}$, 1H), 4.77 (t, $J = 7.2 \text{ Hz}$, 2H), 2.16 (m, $J = 7.2 \text{ Hz}$, 2H), 1.39 (m, 4H), 1.28 (m, 4H), 0.88 (t, $J = 6.4 \text{ Hz}$, 3H). ¹³C NMR (50 MHz, CDCl₃): δ 164.78, 150.61, 146.74, 146.13, 145.94, 137.05, 135.78, 128.82, 128.78, 127.46, 125.94, 123.13, 121.54, 53.47, 30.95, 29.15, 25.99, 22.28, 13.82. Anal. Calcd for C₂₀H₂₂N₆: C, 69.34; H, 6.40; N, 24.26. Found: C, 69.01; H, 6.49; N, 24.07.

2-(2-*n*-Octyl-2H-tetrazol-5-yl)-1,10-phenanthroline, L⁸. Yield: 44%. FT-IR (cm⁻¹): 3038 (w), 2954 (s), 2926 (s), 2869 (s), 2851 (s), 1588 (m), 1493 (s), 1468 (m), 1416 (s), 1396 (m), 1352 (s), 1137 (m), 1050 (m), 854 (s), 735 (m). ¹H NMR (200 MHz, CDCl₃): δ 9.25 (dd, $J = 4.4 \text{ Hz}$, 1H), 8.57 (d, $J = 8.6 \text{ Hz}$, 1H), 8.90 (d, $J = 8.2 \text{ Hz}$, 1H), 8.24 (dd, $J = 8.2 \text{ Hz}$, 1H), 7.81 (s, 2H), 7.64 (dd, $J = 8.2 \text{ Hz}$, 1H), 4.77 (t, $J = 7.2 \text{ Hz}$, 2H), 2.16 (m, $J = 7.2 \text{ Hz}$, 2H), 1.27 (m, 10H), 0.87 (t, $J = 6.6 \text{ Hz}$, 3H). ¹³C NMR (50 MHz, CDCl₃): δ 164.76, 150.54, 146.71, 146.08, 145.90, 137.03, 135.80, 128.81, 128.77, 127.44, 125.94, 123.12, 121.53, 53.44, 31.51, 29.14, 28.84, 28.70, 26.26, 22.41, 13.89. Anal. Calcd for C₂₁H₂₄N₆: C, 69.97; H, 6.71; N, 23.32. Found: C, 69.49; H, 6.69; N, 23.54.

(27) (a) Lebreton, L.; Curet, O.; Gueddari, S.; Mazouz, F.; Bernard, S.; Burnstein, C.; Milcent, R. *J. Med. Chem.* **1995**, *38*, 4786. (b) Detert, H.; Schollmeier, D. *Synthesis* **1999**, 999.

(28) Corey, E. J.; Borror, A. L.; Foglia, T. J. *Org. Chem.* **1965**, *30*, 288.

2-(2-*n*-Decyl-2*H*-tetrazol-5-yl)-1,10-phenanthroline, L¹⁰. Yield: 43%. FT-IR (cm⁻¹): 2950 (m), 2923 (s), 2849 (s), 1590 (m), 1494 (m), 1468 (m), 1418 (s), 1396 (m), 1144 (m), 1052 (w), 856 (m), 736 (m). ¹H NMR (200 MHz, CDCl₃): δ 9.24 (dd, *J* = 4.0 Hz, 1H), 8.57 (d, *J* = 8.2 Hz, 1H), 8.41 (d, *J* = 8.6 Hz, 1H), 8.27 (dd, *J* = 8.2 Hz, 1H), 7.83 (s, 2H), 7.67 (dd, *J* = 8.0 Hz, 1H), 4.78 (t, *J* = 7.6 Hz, 2H), 2.16 (m, 2H), 1.25 (m, 14H), 0.87 (t, *J* = 6.4 Hz, 3H). ¹³C NMR (50 MHz, CDCl₃): δ 164.97, 150.51, 146.66, 146.13, 145.96, 137.20, 136.16, 129.02, 128.98, 127.58, 126.15, 123.36, 121.64, 53.56, 31.73, 29.42, 29.33, 29.20, 29.17, 28.76, 26.26, 22.50, 13.94. Anal. Calcd for C₂₃H₂₈N₆: C, 71.10; H, 7.26; N, 21.63. Found: C, 70.55; H, 7.51; N, 19.67.

2-(2-*n*-Dodecyl-2*H*-tetrazol-5-yl)-1,10-phenanthroline, L¹². Yield: 35%. FT-IR (cm⁻¹): 2955 (m), 2923 (s), 2849 (s), 1644 (w), 1561 (m), 1500 (m), 1470 (s), 1420 (s), 1051 (w), 863 (m), 735 (m). ¹H NMR (200 MHz, CDCl₃): δ 9.26 (dd, *J* = 4.2 Hz, 1H), 8.60 (d, *J* = 8.2 Hz, 1H), 8.44 (d, *J* = 8.2 Hz, 1H), 8.29 (dd, *J* = 8.2 Hz, 1H), 7.87 (s, 2H), 7.68 (dd, *J* = 8.0 Hz, 1H), 4.78 (t, *J* = 7.6 Hz, 2H), 2.17 (m, 2H), 1.26 (m, 18H), 0.87 (t, *J* = 6.4 Hz, 3H). ¹³C NMR (50 MHz, CDCl₃): δ 164.87, 150.19, 146.33, 145.86, 145.71, 137.14, 136.26, 128.96, 128.93, 127.48, 126.12, 123.36, 121.51, 53.54, 31.66, 29.36, 29.27, 29.13, 29.09, 28.67, 26.17, 22.43, 13.87. Anal. Calcd for C₂₅H₃₂N₆: C, 72.08; H, 7.74; N, 20.17. Found: C, 71.22; H, 7.66; N, 20.35.

2-(2-*n*-Tetradecyl-2*H*-tetrazol-5-yl)-1,10-phenanthroline, L¹⁴. Yield: 34%. FT-IR (cm⁻¹): 2920 (s), 2850 (s), 1667 (w), 1590 (w), 1498 (m), 1470 (m), 1418 (m), 1147 (w), 855 (m), 738 (m). ¹H NMR (200 MHz, CDCl₃): δ 9.26 (dd, *J* = 4.4 Hz, 1H), 8.59 (d, *J* = 8.4 Hz, 1H), 8.43 (d, *J* = 8.2 Hz, 1H), 8.28 (dd, *J* = 8.2 Hz, 1H), 7.86 (s, 2H), 7.67 (dd, *J* = 8.0 Hz, 1H), 4.77 (t, *J* = 7.2 Hz, 2H), 2.16 (m, 2H), 1.25 (m, 22H), 0.87 (t, *J* = 6.4 Hz, 3H). ¹³C NMR (50 MHz, CDCl₃): δ 164.90, 150.65, 146.80, 146.21, 146.02, 137.13, 135.91, 128.92, 128.87, 127.53, 126.03, 123.21, 121.61, 53.46, 31.71, 29.46, 29.42, 29.39, 29.30, 29.14, 28.72, 26.22, 22.47, 13.90. Anal. Calcd for C₂₇H₃₆N₆: C, 72.94; H, 8.16; N, 18.90. Found: C, 71.59; H, 8.21; N, 18.63.

2-(2-*n*-Hexadecyl-2*H*-tetrazol-5-yl)-1,10-phenanthroline, L¹⁶. Yield: 51%. FT-IR (cm⁻¹): 2919 (s), 2850 (s), 1667 (w), 1499 (w), 1411 (m), 1142 (w), 854 (m), 739 (m). ¹H NMR (200 MHz, CDCl₃): δ 9.36 (dd, *J* = 4.4 Hz, 1H), 8.62 (d, *J* = 8.2 Hz, 1H), 8.46 (d, *J* = 8.2 Hz, 1H), 8.36 (dd, *J* = 8.2 Hz, 1H), 7.90 (s, 2H), 7.73 (dd, *J* = 8.2 Hz, 1H), 4.76 (t, *J* = 7.2 Hz, 2H), 2.16 (m, 2H), 1.38 (m, 2H), 1.25 (m, 24H), 0.87 (t, *J* = 6.2 Hz, 3H). ¹³C NMR (50 MHz, CDCl₃): δ 164.88, 150.47, 146.68, 146.08, 145.91, 137.08, 135.98, 128.89, 128.86, 127.47, 126.03, 123.21, 121.56, 53.44, 31.68, 29.44, 29.40, 29.36, 29.27, 29.12, 29.11, 29.09, 28.68, 26.18, 22.42, 13.85. Anal. Calcd for C₂₉H₄₀N₆: C, 73.69; H, 8.53; N, 17.78. Found: C, 72.92; H, 8.62; N, 16.99.

The following iron(II) complexes, labeled as **a**, **na**, **nb**, **na·S**, and **nb·S** (where *n* is the carbon number of the 2-alkyl chain attached to tetrazole, **na** for compounds containing ClO₄⁻ (except for the case of **a**, [Fe(L⁰)₂]), and **nb** for BF₄⁻ and **S** is the solvent involved), were prepared by three methods. Method I: The methanol solution of the ligand and iron(II) salt was placed separately in the side arms of an H-shaped tube, and the two solutions were carefully linked by methanol to allow slow liquid-to-liquid diffusion. Crystals were formed in several weeks. Method II: The ligand and iron(II) salt were mixed in methanol. The resulting solution was diffused slowly with the vapor of ethyl ether in a sealed vessel. Crystals were formed in several days. Method III: This is similar to method II except the solvent used is acetonitrile.

[Fe(L⁰)₂], a. Method I. Yield: 36%. FT-IR (cm⁻¹): 3046 (w), 1621 (m), 1574 (m), 1536 (m), 1505 (m), 1425 (s), 1401 (m), 1153 (m), 858 (s), 730 (m). Anal. Calcd for C₂₆H₁₄FeN₁₂: C, 56.75; H, 2.56; N, 30.54. Found: C, 55.88; H, 2.82; N, 30.42.

[Fe(L⁰)₂]·CH₃OH, a·CH₃OH. Method I. Yield: 48%. FT-IR (cm⁻¹): 3417 (b), 3054 (m), 1629 (m), 1538 (m), 1431 (s), 1398 (m), 857 (s), 729 (m). Anal. Calcd for C₂₆H₁₄FeN₁₂·CH₃OH: C, 55.69; H, 3.12; N, 28.86. Found: C, 53.04; H, 3.03; N, 28.78.

[Fe(L¹)₂](ClO₄)₂·CH₃OH, 1a·CH₃OH. Method I. Yield: 44%. FT-IR (cm⁻¹): 3548 (w), 3071 (w), 1435 (m), 1093 (s), 861 (m), 729 (m). Anal. Calcd for C₂₈H₂₀Cl₂FeN₁₂O₈·CH₃OH: C, 42.93; H, 2.98; N, 20.72. Found: C, 42.56; H, 3.01; N, 21.02.

[Fe(L¹)₂](BF₄)₂·CH₃OH·CH₃CN, 1b·CH₃OH·CH₃CN. Method III. Yield: 39%. FT-IR (cm⁻¹): 3629 (w), 3089 (w), 2253 (w), 1435 (m), 1066 (s), 862 (m), 731 (m). Anal. Calcd for C₂₈H₂₀B₂F₈FeN₁₂·CH₃OH·CH₃CN: C, 45.02; H, 3.29; N, 22.02. Found: C, 45.66; H, 2.94; N, 23.35.

[Fe(L²)₂](ClO₄)₂·H₂O, 2a·H₂O. Method I. Yield: 39%. FT-IR (cm⁻¹): 3609 (w), 3537 (w), 3076 (w), 2993 (w), 1436 (m), 1090 (s), 859 (m), 730 (m). Anal. Calcd for C₃₀H₂₄Cl₂FeN₁₂O₈·H₂O: C, 43.66; H, 3.18; N, 20.36. Found: C, 43.69; H, 3.16; N, 20.58.

[Fe(L²)₂](BF₄)₂·H₂O, 2b·H₂O. Method I. Yield: 40%. FT-IR (cm⁻¹): 3629 (w), 3557 (w), 3085 (w), 2992 (w), 1438 (m), 1063 (s), 860 (m), 731 (m). Anal. Calcd for C₃₀H₂₄B₂F₈FeN₁₂·H₂O: C, 45.04; H, 3.28; N, 21.01. Found: C, 45.54; H, 3.21; N, 21.53.

[Fe(L³)₂](ClO₄)₂, 3a. Method III. Yield: 65%. FT-IR (cm⁻¹): 3075 (w), 2972 (w), 1437 (m), 1093 (s), 858 (m), 730 (m). Anal. Calcd for C₃₂H₂₈Cl₂FeN₁₂O₈: C, 46.01; H, 3.38; N, 20.12. Found: C, 45.92; H, 3.38; N, 20.25.

[Fe(L³)₂](BF₄)₂, 3b. Method III. Yield: 44%. FT-IR (cm⁻¹): 3079 (w), 2974 (w), 1438 (m), 1059 (s), 858 (m), 731 (m). Anal. Calcd for C₃₂H₂₈B₂F₈FeN₁₂: C, 47.44; H, 3.48; N, 20.75. Found: C, 47.48; H, 3.53; N, 21.11.

[Fe(L⁴)₂](ClO₄)₂, 4a. Method II. Yield: 37%. FT-IR (cm⁻¹): 3074 (w), 2966 (w), 2937 (w), 2875 (w), 1436 (m), 1089 (s), 858 (m), 730 (m). Anal. Calcd for C₃₄H₃₂Cl₂FeN₁₂O₈: C, 47.29; H, 3.74; N, 19.47. Found: C, 47.16; H, 3.73; N, 19.65.

[Fe(L⁴)₂](BF₄)₂, 4b. Method II. Yield: 53%. FT-IR (cm⁻¹): 3088 (w), 2967 (m), 1437 (m), 1055 (s), 864 (m), 731 (m). Anal. Calcd for C₃₄H₃₂B₂F₈FeN₁₂: C, 48.72; H, 3.85; N, 20.05. Found: C, 48.68; H, 3.84; N, 19.76.

[Fe(L⁵)₂](ClO₄)₂·H₂O, 5a·H₂O. Method II. Yield: 37%. FT-IR (cm⁻¹): 3521 (w), 3056 (w), 2956 (w), 1438 (m), 1085 (s), 864 (m), 730 (m). Anal. Calcd for C₃₆H₃₆Cl₂FeN₁₂O₈·H₂O: C, 47.54; H, 4.21; N, 18.48. Found: C, 47.70; H, 4.34; N, 18.68.

[Fe(L⁵)₂](BF₄)₂·H₂O, 5b·H₂O. Method II. Yield: 33%. FT-IR (cm⁻¹): 3629 (w), 3082 (w), 2958 (m), 2858 (w), 1438 (m), 1062 (s), 859 (m), 731 (w). Anal. Calcd for C₃₆H₃₆B₂F₈FeN₁₂·H₂O: C, 48.90; H, 4.33; N, 19.01. Found: C, 49.46; H, 4.12; N, 19.03.

[Fe(L⁶)₂](ClO₄)₂, 6a. Method II. Yield: 61%. FT-IR (cm⁻¹): 3062 (w), 2953 (w), 2930 (w), 2857 (w), 1437 (m), 1096 (s), 862 (m), 730 (m). Anal. Calcd for C₃₈H₄₀Cl₂FeN₁₂O₈: C, 49.63; H, 4.38; N, 18.28. Found: C, 49.53; H, 4.48; N, 18.46.

[Fe(L⁶)₂](BF₄)₂, 6b. Method II. Yield: 22%. FT-IR (cm⁻¹): 3092 (w), 2929 (m), 2855 (w), 1437 (m), 1063 (s), 863 (m), 731 (w). Anal. Calcd for C₃₈H₄₀B₂F₈FeN₁₂: C, 51.04; H, 4.51; N, 18.80. Found: C, 51.05; H, 4.58; N, 19.19.

[Fe(L⁷)₂](ClO₄)₂, 7a. Method II. Yield: 68%. FT-IR (cm⁻¹): 3086 (w), 2927 (m), 2855 (m), 1437 (m), 1094 (s), 862 (m), 731 (m). Anal. Calcd for C₄₀H₄₄Cl₂FeN₁₂O₈: C, 50.70; H, 4.68; N, 17.74. Found: C, 50.64; H, 4.57; N, 17.78.

[Fe(L⁷)₂](BF₄)₂, 7b. Method II. Yield: 48%. FT-IR (cm⁻¹): 3087 (w), 2927 (m), 2855 (m), 1437 (m), 1059 (s), 864 (m), 731 (m).

Table 1. Crystallographic Data and Structure Refinements for **a**, **a**·CH₃OH, **1a**·CH₃OH, **1b**·CH₃OH·CH₃CN, **2a**·H₂O, **2b**·H₂O, **4b**·CH₃OH, **5a**·H₂O, **5b**·H₂O, **6a**, **6b**, **7a**, **7b**, and **16a**^a

complex	a	a	a ·CH ₃ OH	1a ·CH ₃ OH	1b ·CH ₃ OH·CH ₃ CN	2a ·H ₂ O
formula	C ₂₆ H ₁₄ FeN ₁₂	C ₂₆ H ₁₄ FeN ₁₂	C ₂₇ H ₁₈ FeN ₁₂ O	C ₂₉ H ₂₄ C ₁₂ FeN ₁₂ O ₉	C ₃₁ H ₂₇ B ₂ F ₈ FeN ₁₃ O	C ₃₀ H ₂₆ Cl ₂ FeN ₁₂ O ₉
fw	550.34	550.34	582.38	811.35	827.13	825.38
T/K	293(2)	180(2)	293(2)	293(2)	293(2)	293(2)
cryst syst	orthorhombic	orthorhombic	monoclinic	monoclinic	triclinic	triclinic
space group	<i>Pbcn</i>	<i>Pbcn</i>	<i>P2₁/c</i>	<i>P2₁/c</i>	<i>P1</i>	<i>P1</i>
<i>a</i> /Å	14.0448(4)	13.8675(3)	16.9214(5)	19.7302(4)	10.9217(3)	10.7509(3)
<i>b</i> /Å	9.2259(3)	9.3721(2)	18.1578(4)	10.9490(2)	12.2206(3)	10.8452(3)
<i>c</i> /Å	17.0103(7)	16.4788(5)	8.0538(2)	17.1696(3)	14.9706(7)	15.0267(5)
α/deg	90	90	90	90	80.399(1)	75.648(2)
β/deg	90	90	102.672(8)	113.8565(9)	75.572(1)	84.107(2)
γ/deg	90	90	90	90	67.995(1)	83.302(1)
<i>V</i> /Å ³	2204.1(1)	2141.71(9)	2414.3(1)	3392.2(1)	1788.1(1)	1680.82(9)
<i>Z</i>	4	4	4	4	2	2
<i>D_c</i> /Mg m ⁻³	1.658	1.707	1.602	1.604	1.510	1.631
μ/mm ⁻¹	0.732	0.753	0.676	0.675	0.510	0.682
GOF	0.919	1.063	0.965	1.014	0.900	0.958
R1, wR2 [<i>I</i> > 2σ(<i>I</i>)]	0.0373, 0.0768	0.0315, 0.0858	0.0490, 0.1257	0.0603, 0.1539	0.0739, 0.1597	0.0541, 0.1362
R1, wR2 (all data)	0.1039, 0.0905	0.0512, 0.0914	0.1102, 0.1418	0.1395, 0.1796	0.2291, 0.1983	0.1151, 0.1550
complex	2b ·H ₂ O	4b ·CH ₃ OH	5a ·H ₂ O	5b ·H ₂ O	6a	6b
formula	C ₃₀ H ₂₆ B ₂ F ₈ FeN ₁₂ O	C ₃₅ H ₃₆ B ₂ F ₈ FeN ₁₂ O	C ₃₆ H ₃₈ Cl ₂ FeN ₁₂ O ₉	C ₃₆ H ₃₈ B ₂ F ₈ FeN ₁₂ O	C ₃₈ H ₄₀ Cl ₂ FeN ₁₂ O ₈	C ₃₈ H ₄₀ B ₂ F ₈ FeN ₁₂
fw	800.10	870.23	909.53	884.25	919.57	894.29
T/K	293(2)	293(2)	293(2)	293(2)	293(2)	293(2)
cryst syst	triclinic	monoclinic	monoclinic	monoclinic	monoclinic	monoclinic
space group	<i>P1</i>	<i>C2/c</i>	<i>P2₁/c</i>	<i>P2₁/c</i>	<i>C2/c</i>	<i>C2/c</i>
<i>a</i> /Å	10.7053(3)	23.7949(6)	17.5989(4)	17.7559(6)	23.5373(6)	23.2983(6)
<i>b</i> /Å	10.9912(3)	12.3765(4)	15.0090(3)	14.8845(4)	12.1628(5)	12.0762(4)
<i>c</i> /Å	14.9959(5)	18.5437(6)	17.5184(4)	17.4731(5)	18.6877(6)	18.6481(6)
α/deg	76.150(1)	90	90	90	90	90
β/deg	84.200(3)	125.894(2)	117.255(1)	117.690(1)	126.857(2)	126.759(2)
γ/deg	83.298(2)	90	90	90	90	90
<i>V</i> /Å ³	1696.57(9)	4424.0(2)	4113.6(2)	4089.1(2)	4280.6(2)	4203.5(2)
<i>Z</i>	2	4	4	4	4	4
<i>D_c</i> /Mg m ⁻³	1.566	1.306	1.469	1.436	1.427	1.413
μ/mm ⁻¹	0.536	0.417	0.565	0.452	0.542	0.439
GOF	0.905	1.050	0.939	0.880	0.918	0.913
R1, wR2 [<i>I</i> > 2σ(<i>I</i>)]	0.0588, 0.1290	0.0843, 0.2611	0.0518, 0.1303	0.0797, 0.1308	0.0499, 0.1158	0.0511, 0.1046
R1, wR2 (all data)	0.1713, 0.1563	0.1242, 0.2851	0.1443, 0.1585	0.2930, 0.1746	0.1293, 0.1376	0.1174, 0.1217
complex	7a	7b	16a	16a		
formula	C ₄₀ H ₄₄ Cl ₂ FeN ₁₂ O ₈	C ₄₀ H ₄₄ B ₂ F ₈ FeN ₁₂	C ₅₈ H ₈₀ Cl ₂ FeN ₁₂ O ₈	C ₅₈ H ₈₀ Cl ₂ FeN ₁₂ O ₈		
fw	947.62	922.34	1200.09	1200.09		
T/K	293(2)	293(2)	293(2)	205(2)		
cryst syst	monoclinic	monoclinic	triclinic	triclinic		
space group	<i>C2/c</i>	<i>C2/c</i>	<i>P1</i>	<i>P1</i>		
<i>a</i> /Å	23.7115(4)	23.4991(4)	12.6873(3)	12.5561(4)		
<i>b</i> /Å	12.4063(3)	12.3063(3)	10.3056(2)	19.7989(9)		
<i>c</i> /Å	18.5960(6)	18.5483(7)	27.0758(9)	27.644(1)		
α/deg	90	90	102.199(1)	105.500(1)		
β/deg	125.800(1)	125.621(2)	89.681(1)	94.077(2)		
γ/deg	90	90	110.412(1)	106.070(1)		
<i>V</i> /Å ³	4436.9(2)	4360.3(2)	3234.0 (2)	6284.9(5)		
<i>Z</i>	4	4	2	4		
<i>D_c</i> /Mg m ⁻³	1.419	1.405	1.232	1.268		
μ/mm ⁻¹	0.525	0.425	0.375	0.386		
GOF	0.943	0.952	0.898	0.871		
R1, wR2 [<i>I</i> > 2σ(<i>I</i>)]	0.0722, 0.1882	0.0802, 0.2050	0.0813, 0.1843	0.0668, 0.1173		
R1, wR2 (all data)	0.1718, 0.2233	0.1849, 0.2409	0.2555, 0.2367	0.2825, 0.1618		

$$^a \text{R1} = \sum ||F_o| - |F_c|| / \sum |F_o|, \text{wR2} = [\sum w(F_o^2 - F_c^2)^2 / \sum w(F_o^2)^2]^{1/2}.$$

Anal. Calcd for C₄₀H₄₄B₂F₈FeN₁₂: C, 52.09; H, 4.81; N, 18.22. Found: C, 52.01; H, 4.68; N, 18.30.

[Fe(L⁸)₂](ClO₄)₂, **8a**. Method II. Yield: 72%. FT-IR (cm⁻¹): 3084 (w), 2928 (m), 2853 (w), 1437 (m), 1093 (s), 863 (m), 730 (w). Anal. Calcd for C₄₂H₄₈Cl₂FeN₁₂O₈: C, 51.70; H, 4.96; N, 17.23. Found: C, 51.76; H, 5.00; N, 17.35.

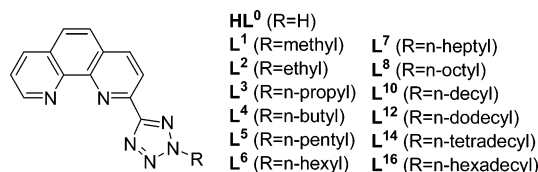
[Fe(L⁸)₂](BF₄)₂, **8b**. Method II. Yield: 57%. FT-IR (cm⁻¹): 3085 (w), 2928 (m), 2854 (m), 1437 (m), 1057 (s), 864 (m), 731 (w).

Anal. Calcd for C₄₂H₄₈B₂F₈FeN₁₂: C, 53.08; H, 5.09; N, 17.69. Found: C, 52.83; H, 5.31; N, 17.46.

[Fe(L¹⁰)₂](ClO₄)₂, **10a**. Method II. Yield: 51%. FT-IR (cm⁻¹): 3074 (w), 2923 (s), 2852 (m), 1437 (m), 1088 (s), 862 (m), 730 (m). Anal. Calcd for C₄₆H₅₆Cl₂FeN₁₂O₈: C, 53.55; H, 5.47; N, 16.29. Found: C, 54.90; H, 5.91; N, 15.04.

[Fe(L¹⁰)₂](BF₄)₂, **10b**. Method II. Yield: 58%. FT-IR (cm⁻¹): 3077 (w), 2925 (s), 2854 (s), 1438 (m), 1063 (s), 862 (m), 731 (w).

Chart 1



(m). Anal. Calcd for $C_{46}H_{56}B_2F_8FeN_{12}$: C, 54.89; H, 5.61; N, 16.70. Found: C, 55.55; H, 6.02; N, 15.39.

[Fe(L^{12}) $_2$](ClO $_4$) $_2$, 12a. Method II. Yield: 55%. FT-IR (cm $^{-1}$): 3072 (w), 2924 (s), 2852 (s), 1437 (m), 1090 (s), 860 (m), 730 (m). Anal. Calcd for $C_{50}H_{64}Cl_2FeN_{12}O_8$: C, 55.20; H, 5.93; N, 15.45. Found: C, 54.63; H, 5.87; N, 15.08.

[Fe(L^{12}) $_2$](BF $_4$) $_2$, 12b. Method II. Yield: 48%. FT-IR (cm $^{-1}$): 3078 (w), 2924 (s), 2854 (s), 1438 (m), 1063 (s), 862 (m), 731 (m). Anal. Calcd for $C_{50}H_{64}B_2F_8FeN_{12}$: C, 56.52; H, 6.07; N, 15.82. Found: C, 55.71; H, 6.23; N, 16.01.

[Fe(L^{14}) $_2$](ClO $_4$) $_2$, 14a. Method II. Yield: 76%. FT-IR (cm $^{-1}$): 3069 (w), 2924 (s), 2853 (s), 1437 (m), 1094 (s), 860 (m), 730 (m). Anal. Calcd for $C_{54}H_{72}Cl_2FeN_{12}O_8$: C, 56.70; H, 6.34; N, 14.69. Found: C, 56.00; H, 6.29; N, 14.56.

[Fe(L^{14}) $_2$](BF $_4$) $_2$, 14b. Method II. Yield: 71%. FT-IR (cm $^{-1}$): 3094 (w), 2923 (s), 2852 (s), 1438 (m), 1064 (s), 871 (m), 731 (m). Anal. Calcd for $C_{54}H_{72}B_2F_8FeN_{12}$: C, 57.98; H, 6.49; N, 15.02. Found: C, 57.51; H, 6.52; N, 14.69.

[Fe(L^{16}) $_2$](ClO $_4$) $_2$, 16a. Method II. Yield: 32%. FT-IR (cm $^{-1}$): 3071 (w), 2924 (s), 2853 (s), 1437 (m), 1093 (s), 860 (m), 730 (m). Anal. Calcd for $C_{58}H_{80}Cl_2FeN_{12}O_8$: C, 58.05; H, 6.72; N, 14.01. Found: C, 58.00; H, 6.67; N, 14.11.

[Fe(L^{16}) $_2$](BF $_4$) $_2$, 16b. Method II. Yield: 63%. FT-IR (cm $^{-1}$): 3095 (w), 2922 (s), 2851 (s), 1468 (m), 1439 (m), 1065 (s), 865 (m), 731 (m). Anal. Calcd for $C_{58}H_{80}B_2F_8FeN_{12}$: C, 59.30; H, 6.86; N, 14.31. Found: C, 58.88; H, 6.99; N, 14.35.

Magnetic Measurements. Magnetic susceptibility measurements were carried out on a Quantum Design MPMS-XL5 SQUID system. Data were collected at 0.1 or 0.2 T in the temperature range between 2 and 400 K. The measurements were performed at a rate of 5 K min $^{-1}$ in both cooling and heating modes. The experimental

susceptibilities were corrected for the diamagnetism of the background of the sample holder and the constituent atoms.^{1g}

X-ray Crystallography. Crystallographic data for single crystals of the compounds were collected^{29a} on a Nonius Kappa CCD diffractometer with a 2.0-kW sealed-tube source using graphite-monochromated Mo K α radiation of $\lambda = 0.71073$ Å and an Oxford low-temperature system. Intensities were corrected for Lorentz and polarization effects and empirical absorption.^{29b} The structures were solved by direct methods and refined by full-matrix least squares against F^2 . Structural calculations were performed using the *SHELX* program.³⁰ All non-hydrogen atoms were refined anisotropically. The hydrogen atoms were added by calculated geometry and not refined. Some constraints were used to model the disorder in solvent molecules and anions.

Mössbauer Spectroscopy. Mössbauer spectra were recorded on an Oxford MS-500 model constant-acceleration spectrometer with a 1024 multichannel analyzer utilizing a room-temperature rhodium matrix cobalt-57 source. The isomer shift values (δ) are with respect to an α -iron foil at room temperature. The variable-temperature spectra were obtained by using an Oxford instrument MD 306 cryostat. This model is capable of changing the temperature in the range of 77–300 K using liquid nitrogen with a variation of 0.5 K. The experimental errors for the isomer shift values, the quadrupole splittings (ΔE_Q), and the line widths (Γ) are less than 0.03 mm s $^{-1}$.

Results

Syntheses. The synthetic routes to obtaining a functional tetrazole ring are mainly two. One is the reaction of amine, sodium azide, and triethyl orthoformate to afford 1-substituted tetrazole.³¹ The other is the reaction of nitrile, sodium azide, and zinc bromide (or ammonium chloride) to afford 5-substituted tetrazole, which is used to synthesize HL^0 .³² The tetrazole ring of HL^0 exhibits a relatively high acidity and can be modified further with alkyl bromide to produce 2-alkyl-5-aryltetrazole (L^n ; Chart 1). Theoretically, its isomeric 1-alkyl-5-aryltetrazole would be formed simultaneously. However, in our case, only the 2-alkyl-5-aryltetra-

Table 2. Important Bond Lengths (Å) for **a**, **a**·CH $_3$ OH, **1a**·CH $_3$ OH, **1b**·CH $_3$ OH·CH $_3$ CN, **2a**·H $_2$ O, **2b**·H $_2$ O, **4b**·CH $_3$ OH, **5a**·H $_2$ O, **5b**·H $_2$ O, **6a**, **6b**, **7a**, **7b**, and **16a**

	a (293 K)	a (180 K)	a ·CH $_3$ OH	1a ·CH $_3$ OH	1b ·solvent	2a ·H $_2$ O
Fe–N1	2.265(2)	2.016(2)	1.998(3)	2.003(3) (Fe1)	1.999(4)	1.999(3)
Fe–N2	2.121(2)	1.906(2)	1.893(2)	1.912(3) (Fe1)	1.892(4)	1.905(2)
Fe–N3	2.168(2)	1.987(1)	1.984(3)	1.993(3) (Fe1)	1.981(4)	1.989(3)
Fe–N7			2.008(2)	2.002(3) (Fe2)	1.990(4)	2.006(3)
Fe–N8			1.894(2)	1.910(3) (Fe2)	1.899(4)	1.904(2)
Fe–N9			1.973(2)	2.000(3) (Fe2)	1.978(5)	1.979(2)
	2b ·H $_2$ O	4b ·CH $_3$ OH	5a ·H $_2$ O	5b ·H $_2$ O	6a	6b
Fe–N1	2.033(3)	2.000(4)	1.993(3)	2.013(4)	1.994(2)	1.991(3)
Fe–N2	1.952(3)	1.904(4)	1.900(2)	1.905(4)	1.896(2)	1.895(3)
Fe–N3	2.031(3)	1.973(4)	1.961(3)	1.988(4)	1.953(2)	1.951(3)
Fe–N7	2.039(3)		2.006(3)	1.994(4)		
Fe–N8	1.952(3)		1.903(2)	1.891(4)		
Fe–N9	2.036(3)		1.990(3)	1.958(4)		
	7a	7b	16a (293 K)	16a (205 K)		
Fe–N1	1.993(4)	1.996(5)	2.161(5)	2.190(5) (Fe1)	2.008(5) (Fe2)	
Fe–N2	1.899(4)	1.901(4)	2.084(5)	2.100(5) (Fe1)	1.921(5) (Fe2)	
Fe–N3	1.964(4)	1.956(5)	2.196(6)	2.226(6) (Fe1)	1.990(5) (Fe2)	
Fe–N7			2.151(5)	2.185(5) (Fe1)	1.999(5) (Fe2)	
Fe–N8			2.090(5)	2.099(5) (Fe1)	1.911(5) (Fe2)	
Fe–N9			2.178(5)	2.217(5) (Fe1)	1.978(5) (Fe2)	

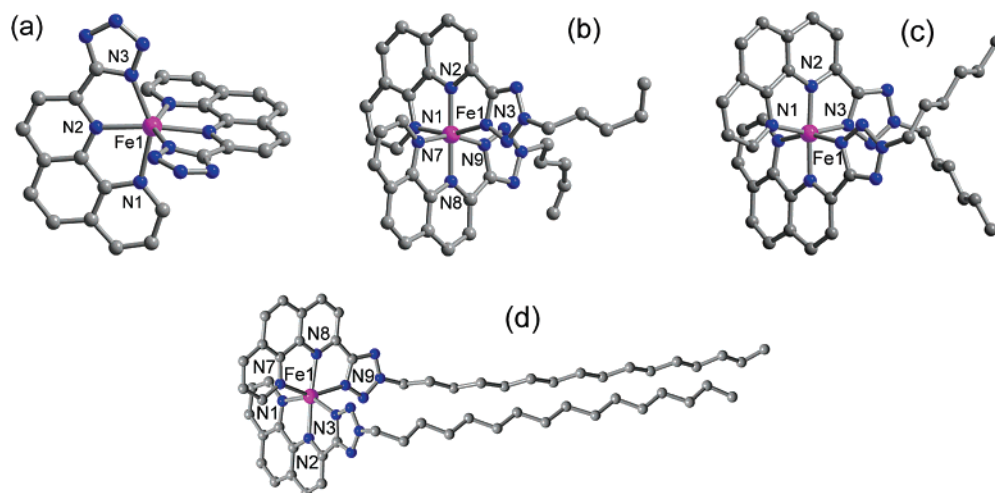


Figure 1. Selected molecular structures of (a) **a**, (b) **5a**·H₂O, (c) **6a**, and (d) **16a** at 293 K.

zole isomer was obtained, which is believed to be the result of the steric effect of the adjacent rigid phenanthroline ring on the 1*H*-site of the tetrazole ring.

The iron(II) complexes were prepared by a slow diffusion method. With the increase of the length of the alkyl chain, the solubility of **Lⁿ** increases in methanol and so does that of the corresponding complexes. The tetrafluoroborate complex **nb** always exhibits a relatively higher solubility than its perchlorate counterpart **na**.

Solid-State Structures. Crystal structures of **a**, **a**·CH₃OH, **1a**·CH₃OH, **1b**·CH₃OH·CH₃CN, **2a**·H₂O, **2b**·H₂O, **4b**·CH₃OH, **5a**·H₂O, **5b**·H₂O, **6a**, **6b**, **7a**, **7b**, and **16a** were determined by single-crystal X-ray diffractometry. Crystallography data and selected molecular geometries are presented in Tables 1 and 2, respectively. The basic molecular moiety of these compounds, as expected, is the distorted octahedral Fe^{II} core chelated by two unsymmetric tridentate 2-tetrazolyl-1,10-phenanthroline ligands in *mer* mode (Figure 1).³³ The equivalent enantiomers formed with Δ and Λ configurations occupy the centrosymmetric lattice. At room temperature, **a** and **16a** have Fe–N distances (2.08–2.27 Å) characterizing HS Fe^{II}, while other compounds have the values (1.89–2.04 Å) for LS Fe^{II}.¹⁴ These agree with the spin states of Fe^{II} of these compounds magnetically measured at room temperature (*vide infra*). The two nearly planar chelating aromatic rings are perpendicular to each other. Because the [Fe(Lⁿ)₂] moiety has two large planar aromatic leafs, the attractive aryl motifs or embrace, proposed by Dance et al.,³⁴ are among the key factors governing the

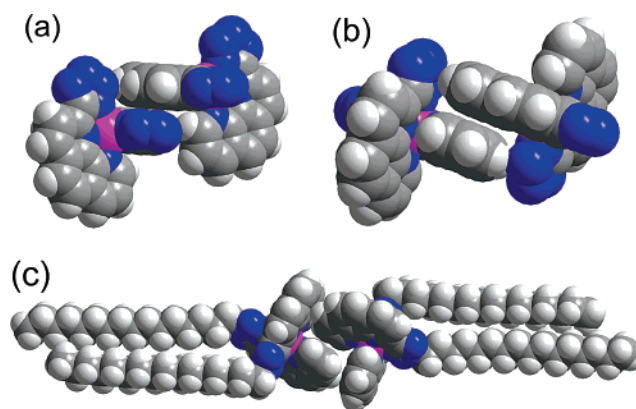


Figure 2. OFF (a) and EF (c) motifs and P4AE-like embrace (b) observed in the serial compounds.

molecular packing and intermolecular interaction in the solid state, which are closely related to the SCO behaviors of these compounds. The serial compounds show motifs of OFF (offset face-to-face), EF (edge-to-face), and/or P4AE (parallel 4-fold aryl embrace, comprised of one OFF and two EF) like, which are all of the combination of π – π stacking and short contact interactions, as depicted in Figure 2, though some delicate differences are observed from compound to compound. More structure details concerning the specific compounds are given below.

The crystal structure of **a** was determined at 293 and 180 K (Table 1), corresponding to the HS and LS states (*vide infra*), respectively. Both structures belong to the same orthorhombic space group *Pbcn*, being isostructural. The Fe^{II} center is a distorted octahedron (Figure 1a). At 293 K, the three unique Fe–N bond distances are 2.265(2), 2.121(2), and 2.168(2) Å, while at 180 K, they decrease to 2.016(2), 1.906(2), and 1.987(1) Å, with an average shortening of the bond length of about 0.2 Å (Table 2). This is a typical value for a Fe^{II} SCO system undergoing spin transition from the HS to LS state. The bond angle of N1–Fe–N3 is 159.2°, about 11.4° larger than the one at 293 K (147.8°), indicative of the contraction of the Fe^{II}–N bonds. The molecular

(29) (a) *Collect data collection software*; Nonius BV: Delft, The Netherlands, 1998. (b) *HKL2000 and maXus softwares*; University of Glasgow: Scotland, U.K.; Nonius BV: Delft, The Netherlands; MacScience Co. Ltd.: Yokohama, Japan, 2000.

(30) Sheldrick, G. M. *SHELX-97, Program for Crystal Structure Determination*; University of Göttingen: Göttingen, Germany, 1997.

(31) (a) Franke, P. L.; Haasnoot, J. G.; Zuur, A. P. *Inorg. Chim. Acta* **1982**, 59, 5. (b) Muttenthaler, M.; Bartel, M.; Weinberger, P.; Hilscher, G.; Linert, W. *J. Mol. Struct.* **2005**, 741, 159.

(32) Demko, Z. P.; Sharpless, K. B. *J. Org. Chem.* **2001**, 66, 7945 and references cited therein.

(33) (a) Constable, E. C.; Kulke, T.; Neuburger, M.; Zehnder, M. *New J. Chem.* **1997**, 21, 1091. (b) Alvarez, S. J. *Am. Chem. Soc.* **2003**, 125, 6795.

(34) Russell, V.; Scudder, M.; Dance, I. *J. Chem. Soc., Dalton Trans.* **2001**, 789.

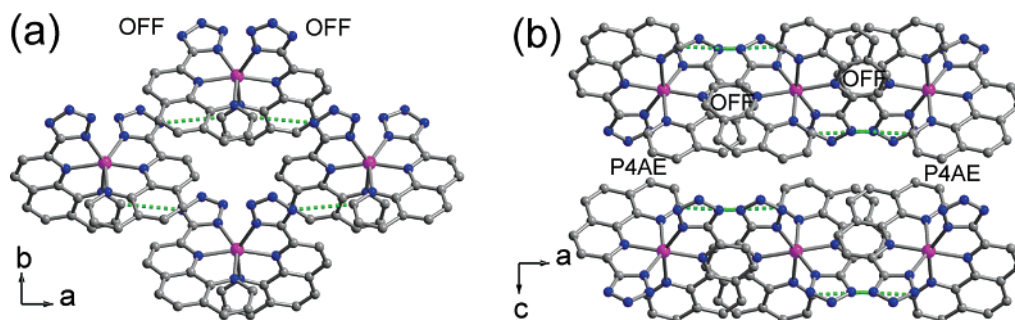


Figure 3. Supramolecular structure of **a** at 293 K with (a) the sheet with molecules in the OFF motif and (b) the stacking of the sheets. Hydrogen-bonding interactions are illustrated as green dashed lines.

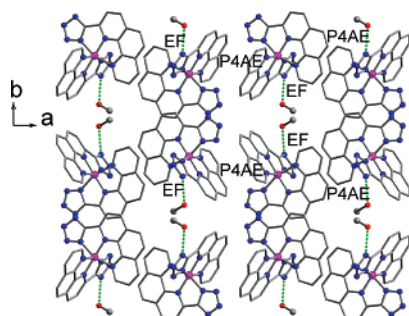


Figure 4. Stacking diagram of **a**·**CH₃OH**. Hydrogen-bonding interactions are illustrated as green dashed lines.

packing in a crystal of **a** can be described as molecular sheets in the *ab* plane further stacking along the *c* direction (Figure 3). Within the sheet, the aryl motif between the molecules is OFF, and the interactions involve the π – π stacking between the face-to-face ligand planes with an average plane–plane distance of 3.411 Å at 293 K and 3.347 Å at 180 K (centroid–centroid distances are 3.578 and 3.621 Å, respectively), and the hydrogen-bonding interaction occurs between the aryl C–H and tetrazolyl N atoms (Table S1, see the Supporting Information). The intersheet motif is P4AE, with an interplane distance of 3.378 Å in the OFF contact and C3H··· π distances of 2.618 Å in the EF one at 293 K. At 180 K, these intersheet geometrical parameters changed much more, corresponding to the largest contraction along the *c* direction (about 0.531 Å; Table 1). These intermolecular interactions are relatively weak but make a 3D-like connection between individual molecules, and this is clearly the reason for a relatively abrupt SCO with a hysteresis loop in **a** (vide infra).

The solvated complex **a**·**CH₃OH** has a packing mode different from that of **a** (Figure 4). It is a monoclinic space group *P*2₁/*c*, exhibiting a lower symmetry than **a**. The Fe–N bond distances are between 1.893(2) and 2.008(3) Å, reflecting the LS Fe^{II} ions in the crystal (Table 2). The molecules form wavy layers via EF and P4AE motifs parallel to the *ac* plane. The lattice methanol molecules locate in the channels running along the *c* direction. Hydrogen-bonding interaction happens between the methanol OH and tetrazolyl N atoms [O1H···N6, 2.911 Å] (Table S1 in the Supporting Information). The inclusion of methanol in **a**·**CH₃OH** lowers the efficient molecular packing and weakens the π – π stacking interaction among the individual [Fe(L⁰)₂] molecules.

The introduction of an alkyl chain into the tetrazole ring strongly affects the crystal packing of the corresponding iron(II) complexes. With an increase of the length of the alkyl chain, the shape of the cationic [Fe(Lⁿ)₂] unit begins to deviate from the spherelike [Fe(L⁰)₂]. Because [Fe(Lⁿ)₂] becomes cationic from L¹, the anions are introduced to keep the charge balance. The introduction of an alkyl chain, solvent, and anion reduces the dimensionality of the interactions through the aryl motifs. In most cases, 1D chains are found. When carbon number *n* is between 1 and 5 (except for **3a**, **3b**, and **4a**), solvent molecules are always included in the lattices to stabilize the crystallization. Because *n* is larger than 5, the alkyl chains play a predominant role in the crystal packing and exclude the solvent molecules in crystal lattices.

For **1a**·**CH₃OH**, there are two different Fe^{II} sites in the unit cell at 293 K (Figure 5a). While the Fe–N bond lengths of 1.910(3) and 2.003(3) Å are very similar around the two sites, the [Fe1(L¹)₂] and [Fe2(L¹)₂] units form 1D chains along the *c* axis alternatively, by an intrachain OFF aryl motif (Table S2 in the Supporting Information). In the [Fe1(L¹)₂]_n chain, the neighboring [Fe1(L¹)₂] cations have π – π stacking between the phenanthroline rings. The [Fe2(L¹)₂]_n chain is similar with slightly different interaction geometries. The [Fe(L¹)₂]_n chains, running along the *c* axis, are packed in a hexagonal style. The anions and solvent molecules are located between the chains. Hydrogen-bonding interaction occurs between the perchlorate O atoms and the aryl and alkyl CH groups.

In **1b**·**CH₃OH**·**CH₃CN**, the strong and weak OFF interactions occur, in turn, between two neighboring phenanthroline rings (Table S2 in the Supporting Information), affording a wavy 1D chain along the *c* + *b* direction (Figure 5b). Additionally, the N atom of the acetonitrile has a hydrogen-bonding interaction with the aryl H atom [C20H···N13 (#: *x*, *y* – 1, *z*) = 3.429 Å (150.4°)], while the methanol molecules do not.

At 293 K, the Fe^{II} ions in **4b**·**CH₃OH** are obviously in the LS state because the bond lengths of Fe–N are between 1.904(4) and 2.000(4) Å (Figure 5d). The two *n*-butyl chains of the cation extend toward each other from the tetrazole rings with the disordered terminal C atoms. The Fe^{II} cations stack into a 1D chain along the *c* axis via OFF interactions. The anions take part in the hydrogen-bonding interactions with aryl CH atoms [C8H···F2 (#: 1 – *x*, 2 – *y*, 2 – *z*) =

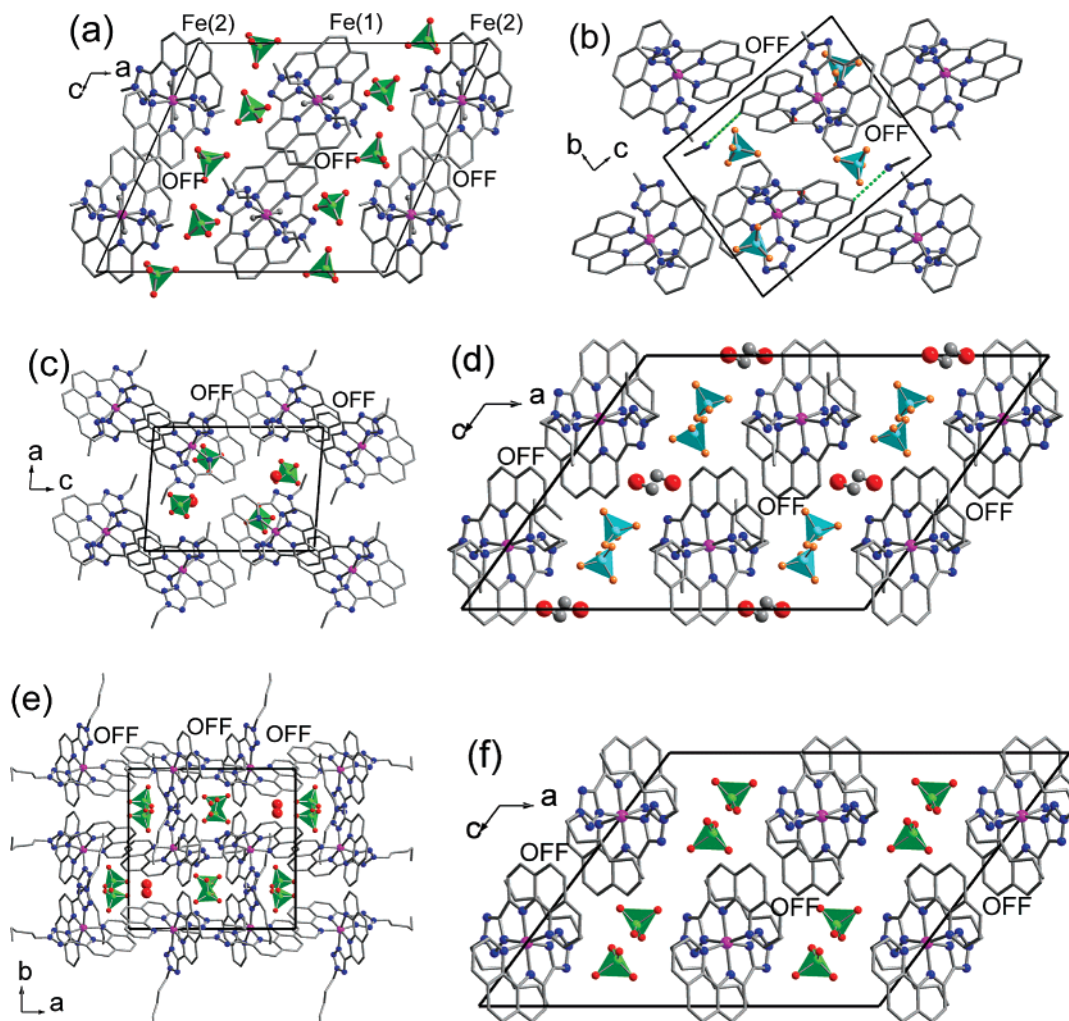


Figure 5. Crystal packing structures of (a) **1a**·CH₃OH, (b) **1b**·CH₃OH·CH₃CN, (c) **2a**·H₂O, (d) **4b**·CH₃OH, (e) **5a**·H₂O, and (f) **6a**.

3.249 Å (145.2°); C3H#···F3 (#: $\frac{1}{2} - x, y - \frac{1}{2}, \frac{3}{2} - z$) = 3.431 Å (157.6°)]. It is worth mentioning that methanol molecules in the lattice have no interactions with other components, which perhaps explains why the crystals are labile to effloresce when exposed to air. Unfortunately, the detailed single-crystal structure of the desolvated sample **4b** cannot be obtained, so a correlation between the structure and the two-step SCO of **4b** is not directly accessible (vide infra). The PXRD measurement of **4b** shows that it has evident differences from the solvated crystal sample **4b**·CH₃OH (Figure S1, see the Supporting Information).

The four pairs, i.e., **2a**·H₂O and **2b**·H₂O, **5a**·H₂O and **5b**·H₂O, **6a** and **6b**, and **7a** and **7b**, are isomorphic in each pair, respectively. The common feature among these complexes is the existence of 1D chains in the lattice, which are formed via the OFF stacking interactions between every two neighboring cations. Hydrogen-bonding interactions are widely found among the anions, solvents, and the aryl and alkyl CH groups.

The crystal structures of **2a**·H₂O and **2b**·H₂O are very similar to each other at 293 K except for some slight differences in crystallographic data. The bond lengths of Fe–N of the two complexes fall in the range of 1.904(2)–2.039(3) Å, indicating the existence of the LS Fe^{II} ions. Wavy

1D chains along the *c* axis are formed, in which the neighboring aryl rings are linked via two alternate OFF interactions with different plane–plane distances, i.e., 3.425 and 3.519 Å in **2a**·H₂O and 3.463 and 3.553 Å in **2b**·H₂O (Figures 5c and S2a in the Supporting Information). Hydrogen-bonding interactions occur among the O atoms of water and aryl and alkyl CH groups [**2a**·H₂O, C17H···O9 = 3.338 Å (166.6°), C29H···O9 = 3.429 Å (163.2°); **2b**·H₂O, C2H···O1 = 3.329 Å (161.4°), C14H···O1 = 3.511 Å (158.4°)]. The anions in the two complexes all participate in the short contacts with aryl and alkyl CH groups (Table S3 in the Supporting Information).

In the pair of **5a**·H₂O and **5b**·H₂O, the OFF interactions between two neighboring aryl rings are nearly the same, with an average plane–plane distance of 3.474 Å. The resulting 1D chains stack along the *a* + *c* direction (Figures 5e and S2b in the Supporting Information). In both of the complexes, the anions have hydrogen-bonding interactions with the CH groups (Table S4 in the Supporting Information). As to the water molecule, it takes part in hydrogen-bonding interactions in **5a**·H₂O [C2H#···O9 (#: $-x, \frac{1}{2} + y, \frac{1}{2} - z$) = 3.722 Å (136.6°)] but not in **5b**·H₂O, which is believed to be the reason that causes totally different SCO behaviors in the two complexes (vide infra). **5a**·H₂O and **5b**·H₂O constitute a

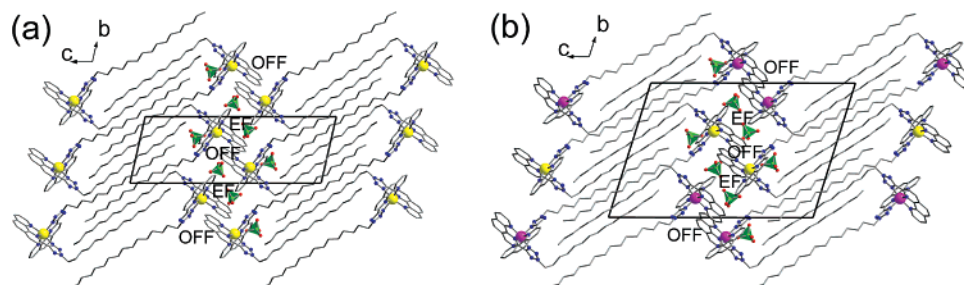


Figure 6. Stacking diagrams of **16a** at (a) 293 K and (b) 205 K (sphere color: yellow for HS FeI; purple for LS Fe2).

unique pair to illustrate how the difference of the anions in crystal packing results in the great difference in SCO behaviors.

6a, **6b**, **7a**, and **7b** are isostructural, all belonging to the same monoclinic space group $C2/c$ (Table 1). The Fe^{II} ions all stay in the LS state with an average $\text{Fe}-\text{N}$ bond length of 1.95 Å. The two alkyl chains of the cations extend their way to each other in a regular zigzag conformation (Figures 1c, 5f, S2c–e in the Supporting Information). The most striking feature of the cations is the helical-like structure, which favors a tight wrap of the two ligands around the Fe^{II} center and thus minimizes the volume of the cation. This may explain why these complexes remain in the LS state in the temperature range of 2–400 K. Beyond the molecular level, 1D chains along the c direction appear in each of these complexes. The order of the strength of the OFF interactions is found as **6a** < **6b** < **7a** < **7b** (Table S5 in the Supporting Information), which simply arises from the relative change of the volumes of the cation and anion.

The crystal structure of **16a** was investigated at 293 (Figure 1d), 205, and 106 K, which correspond to the HS, intermediate, and LS phases in the observed two-step SCO, respectively (vide infra). **16a** crystallizes in the triclinic space group $P\bar{1}$ at the three temperatures. At 293 K, the cell volume is 3234.0(2) Å³ and contains two molecules related by inversion. The bond lengths of the Fe^{II} ion and six N atoms vary in the range of 2.084(5)–2.196(6) Å, indicating HS Fe^{II} sites. At 205 K, the cell doubles and contains four molecules. From the structure, it is evident that one of the two unique Fe^{II} ions, Fe2, experiences SCO from the HS to LS state and the other Fe^{II} ion, Fe1, still remains at the HS state. The $\text{Fe}-\text{N}$ bond lengths show the typical values for the LS Fe2 [1.911(5)–2.008(5) Å] and the HS Fe1 [2.099(5)–2.226(6) Å]. Unfortunately, the quality of the crystallographic data of **16a** becomes poor at 106 K. The crystal structure cannot be fully solved. However, the cell parameters³⁵ have proved that the cell recovers to the state like the one at 293 K; that is, the cell volume changes to 3060.0(3) Å³ and again contains only two molecules. This indicates that all of the Fe^{II} ions in the crystal have transformed to the LS state. The changes of the crystal structures at different temperatures are in accordance with the following thermal analysis (Figure S5i in the Supporting Information).

16a shows two remarkable structural features. One is the U shape of $[\text{Fe}(\text{L}^{16})_2]$, in which the two ordered, rodlike alkyl chains of $n\text{-C}_{16}\text{H}_{33}$ are almost parallel to each other and point in the same direction (Figure 1d). The other is the packing in crystal (Figure 6). The alkyl chains of $[\text{Fe}(\text{L}^{16})_2]$ units in the opposite direction interdigitate, resulting in a structure with alternatively arranged layers of hydrophobic alkyl chains of a thickness of ca. 26 Å and ionic layers consisting of the ClO_4^- anions and the coordinated cationic heads, which are involved in aryl motifs of OFF and EF.

Within the crystal structure of **16a**, different interactions among the ligands and the perchlorate anions are observed, which would be responsible for the occurrence of the two-step SCO with a small hysteresis loop (Table S6 in the Supporting Information). The alternative OFF and EF motifs link the adjacent aryl rings as a chain extending in the ab plane. At 205 K, EF motifs occur between adjacent chains. The two anions locate closely to the Fe^{II} center in two different sites. Cl1O_4^- is closer to the phenanthroline rings than Cl2O_4^- . The O atoms of the perchlorates participate in hydrogen-bonding interaction and short contact with the surrounding phenanthroline rings and alkyl chains at different temperatures.

Magnetic and Thermal Studies. The temperature dependence of the magnetic susceptibility for the crystalline or powder samples of the compounds was measured in the temperature range of 2–400 K, and the results are presented in the form of χ_{MT} vs T curves in Figures 7 and S3 in the Supporting Information and summarized in Table 3. Diverse SCO behaviors have been found in this series, indicating the complication and difficulty of SCO tuning. These SCO complexes can be roughly divided into five groups according to their magnetic properties.

The first one includes **a**, **3a**, **3b**, **4a**, and **5a**· H_2O . They exhibit one-step and reversible SCO behaviors. **a** exhibits a sharp SCO behavior in the range of 230–270 K (Figure 7a). The χ_{MT} value is 3.03 cm³ K mol^{−1} at 300 K. Upon cooling, χ_{MT} remains constant down to 260 K, then drops rapidly, and reaches the LS state at 240 K with $T_{1/2,1}^{\dagger} = 252$ K. The χ_{MT} value is 0.34 cm³ K mol^{−1} at 240 K, showing the transition from the HS to LS state. It decreases continuously to 0.21 cm³ K mol^{−1} at 100 K. Upon heating, χ_{MT} remains almost constant from 100 to 240 K and then increases sharply in the range of 240–265 K with $T_{1/2,1}^{\dagger} = 258$ K. The small hysteresis loop of $\Delta T = 6$ K and the sharp SCO indicate the cooperative character of the transition due to the intermo-

(35) Cell parameters for **16a** at 106 K: triclinic, $P\bar{1}$, $a = 12.4327(5)$ Å, $b = 10.1524(5)$ Å, $c = 25.909(2)$ Å, $\alpha = 89.294(1)^\circ$, $\beta = 88.015(2)^\circ$, $\gamma = 69.431(2)^\circ$, $V = 3060.0(3)$ Å³, $Z = 2$.

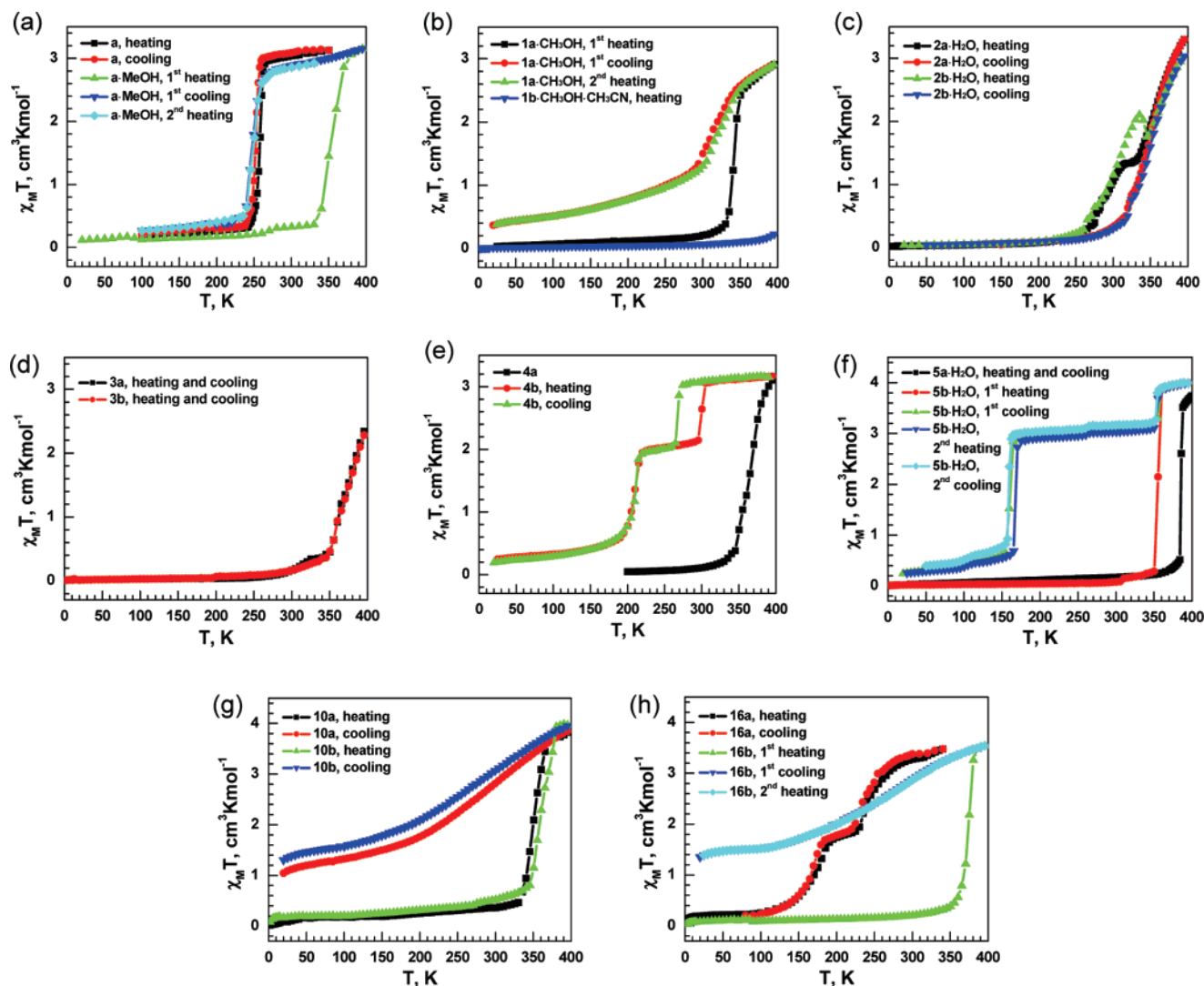


Figure 7. $\chi_M T$ vs T plots for (a) **a** and **a**·CH₃OH, (b) **1a**·CH₃OH and **1a**·CH₃OH·CH₃CN, (c) **2a**·H₂O and **2b**·H₂O, (d) **3a** and **3b**, (e) **4a** and **4b**, (f) **5a**·H₂O and **5b**·H₂O, (g) **10a** and **10b**, and (h) **16a** and **16b**. The lines are guides to the eye.

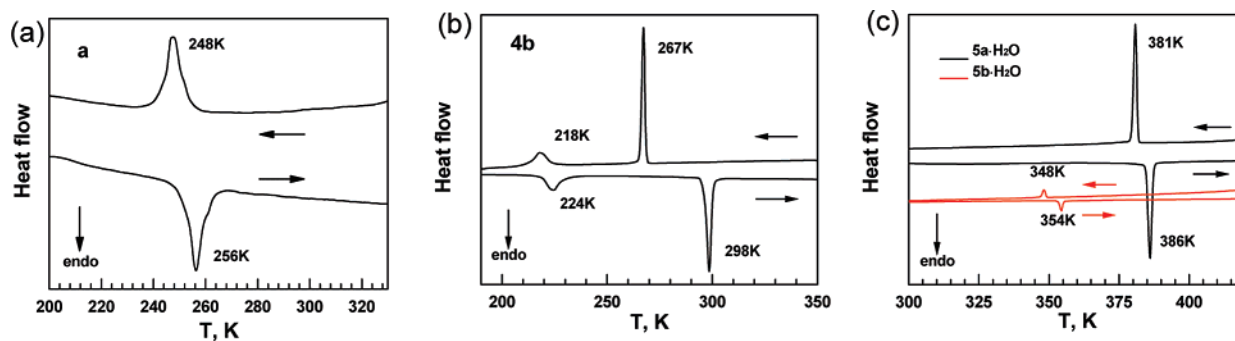


Figure 8. DSC for (a) **a**, (b) **4b**, and (c) **5a**·H₂O and **5b**·H₂O.

lecular interactions in the crystalline sample, which has been clearly revealed by the single-crystal X-ray structure. **3a**, **3b**, **4a**, and **5a**·H₂O display similar one-step and reversible SCO behaviors with higher transition temperatures above 350 K, but having weakened sharpness and no hysteresis for the transitions (Figure 7d–f). DSC measurement for **a** clearly confirms the SCO transition by endothermic and exothermic peaks at ca. 250 K upon heating and cooling (Figure 8a and Table 3). However, the DSC data of **3a**, **3b**, and **4a** display

illegible broad peaks at about 350 K. The TGA curve of **5a**·H₂O shows no discernible loss of solvent below 450 K, and the DSC peaks around 385 K agree well with the SCO transition.

The second group includes **a**·CH₃OH, **1a**·CH₃OH, **2a**·H₂O, **2b**·H₂O, and **5b**·H₂O (Figure 7a–c,f). As they undergo solvent loss upon heating, these complexes show irreversible and complicated SCO behaviors. **a**·CH₃OH is here discussed as a representative. Upon heating, the $\chi_M T$ value exhibits a

Table 3. Summation of Critical Transition Temperature $T_{1/2}$ (K) and Thermal Data ΔH (kJ mol⁻¹) and ΔS (J K⁻¹ mol⁻¹) of **a**, **a**·CH₃OH, **1a**·CH₃OH, **2a**·H₂O, **2b**·H₂O, **3a**, **3b**, **4a**, **4b**, **5a**·H₂O, **5b**·H₂O, **10a**, **10b**, **12a**, **12b**, **14a**, **14b**, **16a**, and **16b**

	a	a·CH₃OH	1a·CH₃OH	2a·H₂O	2b·H₂O	5a·H₂O	5b·H₂O		
$T_{1/2,1}^{\uparrow a}$ ($T_1^{\uparrow b}$)	258 (256) ^d	354	341			386 (386)	356		
$T_{1/2,1}^{\uparrow}$ (T_1^{\uparrow})	252 (248)	249 (244)	310 (309)	349 (343)	349 (346)	386 (381)	160, 355 (348)		
$T_{1/2,2}^{\uparrow}$ (T_2^{\uparrow})		249 (251)	320 (323)	349 (354)	349 (344)		170, 355 (354)		
ΔH_1^{\uparrow} (ΔS_1^{\uparrow}) ^c	11 (41)					25 (65)			
ΔH_1^{\uparrow} (ΔS_1^{\uparrow})	9.9 (40)	9.0 (37)				26 (68)	4.1 (12)		
ΔH_2^{\uparrow} (ΔS_2^{\uparrow})		8.0 (32)					5.1 (15)		
	3a	3b	4a	10a	10b	12a	12b	14a	14b
$T_{1/2,1}^{\uparrow}$ (T_1^{\uparrow})	375	377	365	350	360 (384)	348	374 (382)	366 (373)	371 (388)
$T_{1/2,1}^{\uparrow}$ (T_1^{\uparrow})	375	377	365	290	274	289	277	276	274
$T_{1/2,2}^{\uparrow}$ (T_2^{\uparrow})				290	274	289	277	276	274
ΔH_1^{\uparrow} (ΔS_1^{\uparrow})					38 (100) ^e		35 (92) ^e	30 (80) ^e	40 (102) ^e
	4b			16a			16b		
$T_{1/2,1}^{\uparrow}$ (T_1^{\uparrow})	210 (224), 300 (298)			170 (178), 245 (237)			373 (379)		
$T_{1/2,1}^{\uparrow}$ (T_1^{\uparrow})	210 (218), 268 (267)			165, 240			262		
$T_{1/2,2}^{\uparrow}$ (T_2^{\uparrow})							262		
ΔH_1^{\uparrow} (ΔS_1^{\uparrow})	4.1 (19), 11 (37)			1.7 (9.4), 2.1 (8.7)			37 (96) ^e		
ΔH_1^{\uparrow} (ΔS_1^{\uparrow})	3.6 (16), 11 (41)								

^a $T_{1/2,1}^{\uparrow}$ and $T_{1/2,1}^{\uparrow}$ are the critical transition temperatures in the first heating–cooling cycle, while $T_{1/2,2}^{\uparrow}$ is the one of the heating step in the second cycle. ^b T_1^{\uparrow} , T_1^{\uparrow} , and T_2^{\uparrow} are the temperatures recorded from DSC measurements corresponding to the spin transitions. ^c ΔH_1 and ΔS_1 are the values of the variations of enthalpy and entropy measured at T_1 , and so are ΔH_2 and ΔS_2 . ^d The discrepancies in the $T_{1/2}$ values reported from magnetic susceptibility and those reported from DSC measurements should arise from the different measuring conditions, such as a dinitrogen gas flow always being accompanied in DSC measurements. ^e The relatively large values might include the contribution from the long alkyl side chains.

slow increase from 0.11 cm³ K mol⁻¹ at 20 K to 0.36 cm³ K mol⁻¹ at 330 K. Then it increases quickly to 3.10 cm³ K mol⁻¹ at 385 K with $T_{1/2,1}^{\uparrow} = 354$ K. Upon cooling, the χ_{MT} value decreases gradually to 2.79 cm³ K mol⁻¹ at 275 K and quickly drops to 0.50 cm³ K mol⁻¹ at 235 K with $T_{1/2,1}^{\uparrow} = 249$ K. The following warming and cooling curves superpose well with each other. The TGA data of **a**·CH₃OH reveals the loss of solvent molecules above 305 K. The DSC data show a broad endothermic peak at 339 K upon heating, which corresponds well with the loss of solvent (Figure S5a in the Supporting Information). In the following cooling–heating cycles, the exothermic and endothermic peaks appear at 244 and 251 K, respectively, which arise from the desolvated sample of **a**·CH₃OH. It seems to have the same structure as **a** because of the very similar SCO, thermal properties, and PXRD (Figure S4 in the Supporting Information). Unfortunately, in these solvated complexes, once losing solvent molecules, they exhibit an irreversible desolvation process.

While the SCO property of **1a**·CH₃OH is quite similar to that of **a**·CH₃OH, **2a**·H₂O, **2b**·H₂O, and **5b**·H₂O in this group show more complicated behaviors. **2a**·H₂O and **2b**·H₂O behave similarly, showing two-step transitions in the virgin heating procedure upon desolvation and then one-step transitions in the following cycle for the desolvated phases (**2a** and **2b**). Also the transition temperature for the desolvated phases is higher than that of the solvated phases, reverse to what was observed for **a**·CH₃OH. This is a quite unusual phenomenon because the solvent usually raises the transition temperature in most cases.³⁶

As to **5b**·H₂O, upon the virgin heating, it displays a one-step sharp transition at 350 K, accompanied by the desolvation as shown in TGA (Figure S6d in the Supporting Information). In the following cooling–heating cycles, a two-step SCO repeatedly appears, corresponding to the desolvated

sample **5b** (red powder). The high-temperature step appears between 360 and 349 K with variation of χ_{MT} from 3.80 to 3.12 cm³ K mol⁻¹, corresponding to about a 25% conversion of Fe^{II} from the HS to LS state. The value is quite larger than the expected one of 3.0 cm³ K mol⁻¹ for HS Fe^{II}, suggesting the presence of some Fe^{III} impurity possibly resulting from partial oxidation of the sample. The low-temperature step appears between 170 and 155 K with a decrease of χ_{MT} to 0.64 cm³ K mol⁻¹. Then the χ_{MT} value continues to decrease slowly and reaches 0.24 cm³ K mol⁻¹ at 20 K. Furthermore, there appears a hysteresis loop in the lower-temperature step with $\Delta T = 10$ K.

The third group includes **4b** and **16a**, showing reversible two-step transitions. The magnetic measurement of **4b** was performed on the desolvated sample (red powder), which was further dried in a vacuum oven at 350 K for 12 h. The sample shows a unique two-step SCO between 180 and 305 K (Figure 7e). The low-temperature step appears between 150 and 220 K, corresponding to about a 75% conversion of Fe^{II} ions from the LS to HS state. The plateau is observed in the temperature range of 220–295 K. The high-temperature step exhibits a hysteresis loop ($\Delta T = 32$ K), accompanying the transitions between 295 and 305 K on heating and between 262 and 272 K on cooling. It is worth mentioning that the high-temperature step is more abrupt than the low-temperature one. The DSC curve of **4b** conforms well to its SCO behavior, showing proportionally paired endothermic and exothermic peaks at the corresponding high- and low-temperature regions, respectively (Figure 8b).

- (36) (a) Bonhommeau, S.; Molnár, G.; Galet, A.; Zwick, A.; Real, J.-A.; McGarvey, J. J.; Bousseksou, A. *Angew. Chem., Int. Ed.* **2005**, *44*, 4069. (b) Giménez-López, M. C.; Clemente-León, M.; Coronado, E.; Romero, F. M.; Shova, S.; Tuchagues, J.-P. *Eur. J. Inorg. Chem.* **2005**, 2783. (c) Bréfuel, N.; Shova, S.; Lipkowski, J.; Tuchagues, J.-P. *Chem. Mater.* **2006**, *18*, 5467.

16a exhibits a two-step SCO in the temperature range of 100–300 K (Figure 7h). As the temperature increases, the $\chi_M T$ value increases from 0.29 cm³ K mol⁻¹ at 110 K to 1.64 cm³ K mol⁻¹ at 190 K in the low-temperature step, corresponding to a spin transition of about 50% of the Fe^{II} ions from the LS to HS state. A wide plateau is observed between 190 and 225 K. The high-temperature step appears at 310 K with the $\chi_M T$ value from 1.85 cm³ K mol⁻¹ at 225 K to 3.30 cm³ K mol⁻¹, meaning the LS to HS transition of the other 50% of the LS Fe^{II} ions. It is noticeable that a hysteresis loop, though small, appears with a value of $\Delta T = 5$ K, which is perhaps the result of the existing intermolecular interactions as seen in the crystal structures (vide ante). Two endothermic peaks are found in the DSC curve of **16a** at the heating step, fitting well to the two phase transitions of the two-step SCO (Figure S5f in the Supporting Information).

Some iron(II) complexes showing two-step SCOs have been reported recently, including mononuclear,³⁷ dinuclear,³⁸ and polymeric iron(II) complexes.³⁹ The origin of the two-step SCO is usually ascribed to either the existence of two crystallographically inequivalent Fe^{II} sites, which allows the identification of two equally distributed sublattices of molecules in the crystal, or a competition between long-range cooperative and short-range anticooperative interactions in those complexes with only one crystallographically unique iron center. In our study, the occurrence of the two-step SCO is found in **4b**, **5b**·H₂O (after heating), and **16a**. Among them, only **16a** has been analyzed by X-ray crystal structure determinations at different temperatures according to its SCO behavior. **16a** contains only one crystallographically unique

iron center in both the HS and LS states. An intermediate phase is identified in the plateau of the two-step SCO between 190 and 225 K. The sequence of the HS, the intermediate, and the LS phases has been characterized as “re-entrant” in the sense that the unit cell corresponding to the HS phase is similar to that of the LS phase but differs from the intermediate phase. Such a behavior has only been found in the mononuclear complex [Fe(2-pic)₃]Cl₂·EtOH (2-pic = 2-picolyamine) reported by Bürgi and co-workers.^{37d} Compared with other complexes **na** and **nb** (*n* > 8), the two-step SCO in **16a** looks like an exception. Its origin can only be designated to the “correct” packing of the hexadecyl side chains and perchlorate anions in the lattice. **16a** is a good example for a better understanding of the origin of two-step SCO in mononuclear iron(II) complexes.

The fourth one is composed of **10a**, **10b**, **12a**, **12b**, **14a**, **14b**, and **16b** with similar SCO behaviors (Figures 7g and S3 in the Supporting Information). They display relatively sharp and complete LS-to-HS transitions in the range of 330–385 K on the first heating procedure and then very gradual and reversible incomplete transitions between 100 and 395 K for further cooling–heating cycles, corresponding to about 50% of the Fe^{II} ions captured in the HS state. The DSC curves of **10a**, **10b**, **12a**, **12b**, **14a**, and **14b** are similar to each other (Figure S5e in the Supporting Information). Upon warming in the first cycle, the broad endothermic peaks appear in the range of 350–400 K, corresponding with the complete spin transitions of the samples.

Although it exhibits SCO properties similar to those of **10a**–**14b**, the DSC measurement of **16b** shows a different thermal behavior (Figure S5g in the Supporting Information). The peak at 379 K is related to the complete SCO of the Fe^{II} ions at the heating step in the first cycle. However, it disappears in the following cooling–heating cycles. Meanwhile, new exothermic and endothermic peaks appear at 316 and 323 K, respectively, which are assigned to a phase transition arising from the long alkyl chains.

Finally, the fifth group includes **1b**·CH₃OH·CH₃CN, **6a**, **6b**, **7a**, **7b**, **8a**, and **8b**, all residing in the LS state in the temperature range of 2–400 K.

Mössbauer Spectroscopy. Mössbauer spectra of **5b** and **16a** recorded at several selected temperatures are shown in Figure 9. The corresponding Mössbauer parameters are given in Table 4.

The Mössbauer spectra of **5b** at 295 and 100 K correspond to the regions of the intermediate and LS states, respectively (Figure 9a). At 295 K, the spectrum consists of one major quadrupole doublet with hyperfine parameters that are indicative of HS Fe^{II} ($\delta = 1.01$ mm s⁻¹; $\Delta E_Q = 1.41$ mm s⁻¹; area = 60.4%) and one minor quadrupole doublet of LS Fe^{II} ($\delta = 0.33$ mm s⁻¹; $\Delta E_Q = 0.96$ mm s⁻¹; area = 39.6%). It is consistent with the magnetic susceptibility measurement reported above (Figure 1h), in which about 25% of the Fe^{II} ions take the spin transition from the HS to LS state in the intermediate state. At 100 K, the area ratio of the two quadrupole doublets of the HS and LS Fe^{II} ions changes to 1:9.5, meaning the predominant existence of the LS Fe^{II} species and a small residual of HS species (9.5%).

- (37) (a) Boinnard, D.; Bousseksou, A.; Dworkin, A.; Savariault, J.-M.; Varret, F.; Tuchagues, J.-P. *Inorg. Chem.* **1994**, *33*, 271. (b) Simaan, A. J.; Boillot, M.-L.; Livi  re, E.; Boussac, A.; Girerd, J.-J. *Angew. Chem., Int. Ed.* **2000**, *39*, 196. (c) Matouzenko, G. S.; L  tard, J.-F.; Lecocq, S.; Bousseksou, A.; Capes, L.; Salmon, L.; Perrin, M.; Kahn, O.; Collet, A. *Eur. J. Inorg. Chem.* **2001**, 2935. (d) Chernyshov, D.; Hostettler, M.; T  rnroos, K. W.; B  rgi, H.-B. *Angew. Chem., Int. Ed.* **2003**, *42*, 3825. (e) Hibbs, W.; van Koningsbruggen, P. J.; Arif, A. M.; Shum, W. W.; Miller, J. S. *Inorg. Chem.* **2003**, *42*, 5645. (f) Sunatsuki, Y.; Ohta, H.; Kojima, M.; Ikuta, Y.; Goto, Y.; Matsumoto, N.; Iijima, S.; Akashi, H.; Kaizaki, S.; Dahan, F.; Tuchagues, J.-P. *Inorg. Chem.* **2004**, *43*, 4154. (g) Yamada, M.; Hagiwara, H.; Torigoe, H.; Matsumoto, N.; Kojima, M.; Dahan, F.; Tuchagues, J.-P.; Re, N.; Iijima, S. *Chem.–Eur. J.* **2006**, *12*, 4536.
- (38) (a) Real, J. A.; Bolvin, H.; Bousseksou, A.; Dworkin, A.; Kahn, O.; Varret, F.; Zarembowitch, J. *J. Am. Chem. Soc.* **1992**, *114*, 4650. (b) L  tard, J.-F.; Real, J. A.; Moliner, N.; Gaspar, A. B.; Capes, L.; Cadot, O.; Kahn, O. *J. Am. Chem. Soc.* **1999**, *121*, 10630. (c) Ksenofontov, V.; Gaspar, A. B.; Niel, V.; Reiman, S.; Real, J. A.; G  tlich, P. *Chem.–Eur. J.* **2004**, *10*, 1291. (d) Nakano, K.; Kawata, S.; Yoneda, K.; Fuyuhira, A.; Yagi, T.; Nasu, S.; Morimoto, S.; Kaizaki, S. *Chem. Commun.* **2004**, 2892. (e) Ortega-Villar, N.; Thompson, A. L.; Mu  oz, M. C.; Ugald  -Sald  var, V. M.; Goeta, A. E.; Moreno-Esparza, R.; Real, J. A. *Chem.–Eur. J.* **2005**, *11*, 5721. (f) Gaspar, A. B.; Mu  oz, M. C.; Real, J. A. *J. Mater. Chem.* **2006**, *16*, 2522 and references cited therein.
- (39) (a) Garcia, Y.; Kahn, O.; Rabardel, L.; Chansou, B.; Salmon, L.; Tuchagues, J.-P. *Inorg. Chem.* **1999**, *38*, 4663. (b) Breuning, E.; Ruben, M.; Lehn, J.-M.; Renz, F.; Garcia, Y.; Ksenofontov, V.; G  tlich, P.; Wegelius, E.; Rissanen, K. *Angew. Chem., Int. Ed.* **2000**, *39*, 2504. (c) Galet, A.; Niel, V.; Mu  oz, M. C.; Real, J. A. *J. Am. Chem. Soc.* **2003**, *125*, 14224. (d) Grunert, C. M.; Schweifer, J.; Weinberger, P.; Linert, W.; Mereiter, K.; Hilscher, G.; Muller, M.; Wiesinger, G.; van Koningsbruggen, P. J. *Inorg. Chem.* **2004**, *43*, 155. (e) Niel, V.; Thompson, A. L.; Goeta, A. E.; Enachescu, C.; Hauser, A.; Galet, A.; Mu  oz, M. C.; Real, J. A. *Chem.–Eur. J.* **2005**, *11*, 2047. (f) Nihei, M.; Ui, M.; Yokota, M.; Han, L.; Maeda, A.; Kishida, H.; Okamoto, H.; Oshio, H. *Angew. Chem., Int. Ed.* **2005**, *44*, 6484.

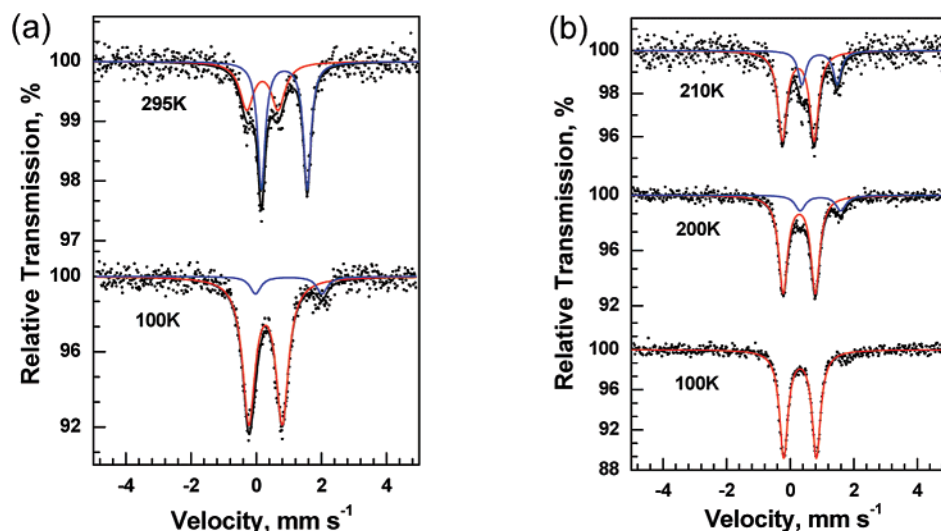


Figure 9. ^{57}Fe Mössbauer spectra of (a) **5b** at 295 and 100 K and (b) **16a** at 210, 200, and 100 K (red line, LS Fe^{II} ; blue line, HS Fe^{II} ; black line, the sum of HS and LS Fe^{II}).

Table 4. Mössbauer Parameters for **5b** and **16a**

complex	T , K	Δ , mm s^{-1}	ΔE_Q , mm s^{-1}	$\Gamma/2$, mm s^{-1}	area, %	assignment
5b	295	1.01	1.41	0.14	60.4	HS
		0.33	0.96	0.26	39.6	LS
	100	1.13	2.04	0.20	9.5	HS
		0.42	1.03	0.23	90.5	LS
16a	210	1.06	1.11	0.15	25.2	HS
		0.39	1.00	0.17	74.8	LS
	200	1.10	1.28	0.20	15.7	HS
		0.43	1.01	0.17	84.3	LS
	100	0.46	1.03	0.16	100	LS

The magnetic susceptibility measurement at this temperature also reveals a residual of about 10% of the HS Fe^{II} ions. These results are in perfect agreement with the magnetic susceptibility measurement that reveal an inequivalent two-step SCO when the sample loses crystallized solvent molecules.

The Mössbauer spectra of **16a** were recorded at 295, 210, 200, and 100 K (Figure 9b). The high-temperature spectrum at 295 K was not well collected because of the high noise of the background. At 210 K, the major and minor quadrupole doublets are designated as LS and HS Fe^{II} unambiguously, with hyperfine parameters of $\delta = 0.39 \text{ mm s}^{-1}$, $\Delta E_Q = 1.00 \text{ mm s}^{-1}$, and area = 74.8% and $\delta = 1.06 \text{ mm s}^{-1}$, $\Delta E_Q = 1.11 \text{ mm s}^{-1}$, and area = 25.2%, respectively. The area ratios of the two quadrupole doublets of the LS and HS Fe^{II} at 210 and 200 K are about 3:1 and 4:1, respectively. Although the two temperatures are in the right region of the intermediate state existing as HS–LS pairs, the corresponding area ratios are deviated from the desired value of 1:1. At 100 K, all of the Fe^{II} ions exist in the LS state, consistent with the magnetic susceptibility measurement.

Discussion and Conclusions

Ligand Effect. Phenanthroline and tetrazole are individually among the most widely used ligands in the construction of SCO systems. Phenanthroline shows a relatively stronger ligand-field strength, which tends to form LS species such

as $[\text{Fe}^{\text{II}}(\text{phen})_3]^{2+}$,⁴⁰ compared with the $T_{1/2}$ between 63 and 204 K of $[\text{Fe}^{\text{II}}(\text{tetrazole})_6]^{2+}$.⁴¹ Rigid phenanthroline plays a role in forming π – π stacking interaction to make SCO abrupt and introduce hysteresis while tetrazole owns a rare site for modification and the left N atoms may be involved in hydrogen-bonding interactions. The successful combination of the two SCO structural units affords us the tridentate N-containing compound 2-(tetrazol-5-yl)-1,10-phenanthroline **HL**⁰ and its alkyl derivatives **L**^{*n*} as SCO ligands with the aim of finely tuning SCO behaviors in iron(II) complexes. As expected, **a** exhibits a SCO in the range of 230–270 K with $T_{1/2}$ at about 255 K, which is obviously lower than $[\text{Fe}^{\text{II}}(\text{phen})_3]^{2+}$ and higher than $[\text{Fe}^{\text{II}}(\text{tetrazole})_6]^{2+}$.

The introduction of an alkyl chain into **HL**⁰ has both electronic and steric effects on the SCO behaviors of the corresponding complexes. Because alkyl chains have a weak tendency to donate electrons, the ligand-field strengths of the alkyl-modified ligands **L**^{*n*} should increase slightly more than **HL**⁰.^{1j} Experimentally, such a modification generally raises $T_{1/2}$ of **na** and **nb** compared with **a**. For example, $T_{1/2}$ is at about 365 K in **4a** and above 400 K in **6a**, **6b**, **7a**, and **7b**. As to the steric effect, the cations in **na** and **nb** have commonly a less efficient packing than **a**, in which the spherelike molecules $[\text{Fe}(\text{L}^0)_2]$ stack tightly to form 2D sheets via OFF motifs.

With an increase of the alkyl-side-chain length, the effect of the alkyl chain on SCO becomes more and more important. It experiences four classes owing to the changes of the conformation of the alkyl chain. In the first class ($n = 1$ –5), the short alkyl chain randomly extends out from the tetrazole ring. Its effect on SCO is often disturbed by anion and solvent molecules. Various types of SCO emerge in this class, such as in **1a**·CH₃OH, **1b**·CH₃OH·CH₃CN, **2a**·H₂O, **4b**·CH₃OH, **5a**·H₂O, and **5b**·H₂O, reflecting the

(40) (a) Zalken, A.; Templeton, D. H.; Ueki, T. *Inorg. Chem.* **1973**, 12, 1641. (b) Fujiwara, T.; Iwamoto, E.; Yamamoto, Y. *Inorg. Chem.* **1984**, 23, 115.

(41) (a) van Koningsbruggen, P. J. *Top. Curr. Chem.* **2004**, 233, 123. (b) Kusz, J.; Gülich, P.; Spiering, H. *Top. Curr. Chem.* **2004**, 234, 129.

competition of the effects of the alkyl chain, anion, and solvent on crystal packing. In the second class ($n = 6-8$), the alkyl chain stretches out from the aryl plane in a rodlike structure. The conformation of the alkyl chain favors a tightly helical-like binding of the ligand with a metal center, which results in the LS state of the Fe^{II} ions in **6a**, **6b**, **7a**, **7b**, **8a**, and **8b**. Solvent molecules are no longer included in the lattice from this class. In the third class ($n = 10-14$), the behaviors of the long alkyl chain itself become overwhelming on SCO properties. After annealing at 400 K, the samples exhibit solution-like reversible SCO behaviors.⁴² Similar gradual and incomplete transitions are found in some complexes bearing long alkyl chains.⁴³ In the final class ($n \geq 16$), the characteristics of liquid crystal begin to emerge owing to the long enough alkyl chain (Figure S7 in the Supporting Information). **16a** surprisingly exhibits a two-step SCO, while **16b** shows a SCO behavior similar to that of **10a-14b**. Further studies will focus on these species to reveal the synergy of SCO and ionic liquid-crystalline properties.⁴⁴

Counterion Effect. Counterions certainly exert an obvious influence on SCO behaviors.^{1h,7} As to ClO₄⁻ and BF₄⁻, the two anions have some similarities, such as having a tetrahedral configuration, involving hydrogen-bonding interaction, and often falling in disorder. Their differences are mainly in the aspects of size and electronic properties. In our study, no striking differences are found in the pairs ($n = 2, 3, 6-8, 10, 12$, and 14). In other pairs ($n = 1, 4$, and 5), the different SCO behaviors most probably originate not from the anion effect but from the solvent effect. As to **16a** and **16b**, they are the only pair showing totally different SCO behaviors excluding the interference of the solvent effect. The crystal structure of **16a** reveals that the perchlorate anions are involved in the interactions with the cations (Table 8). It is reasonable to guess that the proper size and electronic property of the perchlorate anions exerts a delicate influence on crystal packing, through which the two-step SCO is accidentally induced. Certainly, the effect of the alkyl chain cannot be excluded. The investigation using smaller or larger anions such as Cl⁻ or BPh₄⁻ to tune SCO is worth performing later.

Solvent Effect. It has been long recognized that solvent molecules can drastically affect the SCO behaviors of iron(II) complexes.⁸ In our case, **a** and **a·CH₃OH**, **1a·CH₃OH** and **1b·CH₃OH·CH₃CN**, **2a·H₂O** and **2b·H₂O**, and **5a·H₂O** and **5b·H₂O** afford the typical examples to distinguish the solvent effect explicitly. The involvement of solvent mol-

ecules commonly increases $T_{1/2}$ to a higher temperature and even stabilizes LS species within the measured temperature region. For example, **a·CH₃OH** undergoes SCO at $T_{1/2,1}^{\dagger} = 354$ K in the first heating step with a value of about 105 K higher than **a**. Compared with **1a·CH₃OH**, **1b·CH₃OH·CH₃CN** keeps in the LS state up to 400 K. In a special case, **2a·H₂O** and **2b·H₂O** exhibit an abnormal inversion of the values of $T_{1/2,1}^{\dagger}$ and $T_{1/2,1}^{\dagger}$ of the solvated and desolvated species, respectively, around ambient temperature.

Commonly, the loss of solvent molecules causes an irreversible SCO.⁴⁵ In **a·CH₃OH**, **2a·H₂O**, and **2b·H₂O**, the "SCO" is indeed the reflection of the transformation of two species, i.e., the solvated LS one and the desolvated HS one. The temperature range of the occurrence of SCO is rightly the one where the solvated species changes to the desolvated species. Unfortunately, although the solvent effect on SCO has been observed for a long time, the mechanism of how the solvent affects the SCO property remains an enigma.^{8d}

Intermolecular Interactions. As mentioned above, intermolecular interactions in a crystal lattice help to induce an abrupt SCO behavior even with a hysteresis loop. $\pi-\pi$ stacking and hydrogen-bonding interactions widely appear in these compounds. The existence of the large rigid phenanthroline rings favors the formation of OFF, EF, and P4AE stacking interactions, which is responsible for the relatively abrupt transitions such as those in **a** (with a loop of $\Delta T = 6$ K). Hydrogen-bonding interaction occurs among the solvents, anions, tetrazolyl N atoms, and alkyl and aryl CH groups. Seemingly, it exerts an influence on SCO by stabilizing the solvents in a crystal lattice. For example, **1b·CH₃OH·CH₃CN** loses the solvent at a relatively higher temperature, in which the acetonitrile has an interaction with the aryl CH groups. When the solvents do not join hydrogen-bonding interaction, such as in **4b·CH₃OH** and **5b·H₂O**, their crystals are easy to effloresce or lose solvent upon heating.

Acknowledgment. This work was supported by the National Natural Science Foundation of China (Grants 20221101, 20490210, and 20571005), the National Basic Research Program of China (Grant 2006CB601102), and the Research Fund for the Doctoral Program of Higher Education (Grant 20050001002).

Supporting Information Available: Crystallographic data in CIF format and additional magnetic data, crystal packing plots, and thermal data for the complexes in PDF format. This material is available free of charge via the Internet at <http://pubs.acs.org>.

IC062062H

- (42) (a) Telfer, S. G.; Bocquet, B.; Williams, A. F. *Inorg. Chem.* **2001**, *40*, 4818. (b) Fujigaya, T.; Jiang, D.-L.; Aida, T. *J. Am. Chem. Soc.* **2003**, *125*, 14690.
- (43) (a) Galyametdinov, Y.; Ksenofontov, V.; Prosvirin, A.; Ovchinnikov, I.; Ivanova, G.; Gütllich, P.; Haase, W. *Angew. Chem., Int. Ed.* **2001**, *40*, 4269. (b) Hayami, S.; Danjobara, K.; Inoue, K.; Ogawa, Y.; Matsumoto, N.; Maeda, Y. *Adv. Mater.* **2004**, *16*, 869. (c) Seredyuk, M.; Gaspar, A. B.; Ksenofontov, V.; Reiman, S.; Galyametdinov, Y.; Haase, W.; Rentschler, E.; Gütllich, P. *Chem. Mater.* **2006**, *18*, 2513.
- (44) Binnemans, K. *Chem. Rev.* **2005**, *105*, 4148.

- (45) (a) Codjovi, E.; Sommer, L.; Kahn, O.; Jay, C. *New J. Chem.* **1996**, *20*, 503. (b) Garcia, Y.; Koningsbruggen, P. J. V.; Codjovi, E.; Lapouyade, R.; Kahn, O.; Rabardel, L. *J. Mater. Chem.* **1997**, *7*, 857. (c) van Koningsbruggen, P. J.; Garcia, Y.; Codjovi, E.; Lapouyade, R.; Kahn, O.; Fournès, L.; Rabardel, L. *J. Mater. Chem.* **1997**, *7*, 2069. (d) Garcia, Y.; Koningsbruggen, P. J.; Lapouyade, R.; Fournès, L.; Rabardel, L.; Kahn, O.; Ksenofontov, V.; Levchenko, G.; Gütllich, P. *Chem. Mater.* **1998**, *10*, 2426. (e) Hayami, S.; Gu, Z.-Z.; Yoshiki, H.; Fujishima, A.; Sato, O. *J. Am. Chem. Soc.* **2001**, *123*, 11644. (f) Roubeau, O.; Haasnoot, J. G.; Codjovi, E.; Varret, F.; Reedijk, J. *Chem. Mater.* **2002**, *14*, 2559.